The Dissertation Committee for Ramón Carriles Jaimes
certifies that this is the approved version of the following dissertation:

# NONLINEAR OPTICAL CHARACTERIZATION OF Si/HIGH-$\kappa$ DIELECTRIC INTERFACES

Committee:

Michael C. Downer, Supervisor

Alain C. Diebold

John G. Ekerdt

Manfred Fink

Greg O. Sitz

# NONLINEAR OPTICAL CHARACTERIZATION OF Si/HIGH-$\kappa$ DIELECTRIC INTERFACES

**by**

**Ramón Carriles Jaimes, B.S.**

**DISSERTATION**

Presented to the Faculty of the Graduate School of

The University of Texas at Austin

in Partial Fulfillment

of the Requirements

for the Degree of

**DOCTOR OF PHILOSOPHY**

THE UNIVERSITY OF TEXAS AT AUSTIN

December 2005

To my all, God

to my beloved, Estrella

to my joy, Elisa

and to my supportive parents.

# Acknowledgments

Many people contributed to this dissertation in many different ways. By far the most direct contribution came from my supervisor, Prof. Michael C. Downer. He always had useful suggestions and provided insight into every aspect of this work. I learnt much from him, not only about second harmonic generation, but more importantly about scientific and professional life. I also thank my committee members, Drs. Diebold, Ekerdt, Fink, and Sitz, for their time and contributions to this work.

In the lab, many colleagues contributed to make life and things easier with their friendship, support and advice. Among them I owe special thanks to Philip T. Wilson for introducing me to the world of ultrafast optics. On the Epioptics lab I will remember and be grateful to Yingying Jiang, Daeyoung Lim, Jinhee Kwon, Jesse Canterbury, Kui Wu, Lucymarie Mantese, Yongquian An, Peter Figliozzi, Lianfeng Sun, Thomas Pfifer, and Carsten Winterfeldt. I thank also the students in the Terawatt system for their help and many entertaining conversations: Rafal Zgadzaj, Bonggu Shim, Nicholas Matlis, Franklin Grigsby, Benjamin Bowes, Erhard Gaul, Andy Rundquist, P. J Smith, and Peng Dong.

I wish to specially thank my wife, Estrella, for being a continuous source of inspiration and support. I seriously doubt that I could have come this far without her. Our daughter, Elisa, filled us with joy and made the last year of my studies more enjoyable. I deeply thank my parents, Ramón and Esiolat for all their loving support. Also I acknowledge my sisters, Esiolat and Verenice, for their continuous

encouragement. My mother, sister, and brother in Law were always ready to help and support me and my family when in need.

I am very grateful to CONACYT (Concejo Nacional de Ciencia y Tecnología) in Mexico, the Institute of International Education, and the Texas Materials Institute for their financial support at different times during my studies. Special thanks to Jimmy Price and Sematech for providing the high-$\kappa$ samples. James Halligan, Norma Kotz, Olga Vorloou, and Linda Hallidy in the Physics department, and Mary Whitmore, and Lydia Griffith in the Texas Materials Institute were always helpful when traveling, enrolling for a new semester, or dealing with other burocracies. Edwin Baez and Lanny Sandefur in the cryogenics lab, and Jack Clifford in the machine shop gave much needed help and advice.

From my College years I thank Profs. Luis Fernando Urrutia Rios, Hugo Aurelio Morales Tecotl, Alfredo Macías, Roberto Olayo, and Roberto Alexander Katz Kaufman for their teachings, guidance, and support. My good friends Marco Antonio Rodriguez Jimenez, Alfred Barry U'Ren Cortes, Fabian Erasmo Peña Arellano, Jose Agustín Peña Arellano, Luis Agustín Olivarez Quiroz, Felipe Jimenez Angeles, and Eva Hernandez Tellez made those years even more enjoyable.

*Ramón Carriles*

# NONLINEAR OPTICAL CHARACTERIZATION OF Si/HIGH-$\kappa$ DIELECTRIC INTERFACES

Publication No. _____

Ramón Carriles Jaimes, Ph.D.
The University of Texas at Austin, 2005

Supervisor: Michael C. Downer

Sum frequency generation between a Ti:Sapphire beam and white light continuum is performed to obtain spectral information from GaAs(001). The experimental difficulties are analyzed and possible solutions and extensions to the technique proposed. The phase of second harmonic generation (SHG) is measured using a frequency domain technique. Phase shifts in GaAs under azimuthal rotation are observed and explained. The phase of the surface second order susceptibility tensor elements of Si is measured. For the first time SHG phase from $Si/SiO_2$ and $Si/SiO_2$/Hf-silicate is measured with a temporal resolution better than one second. $Si/SiO_2/Hf_{(1-x)}Si_xO_2$ stack structures are studied using rotational anisotropic, spectroscopic, and time dependent SHG. It is found that the signal is affected by Si content ($x$) and by annealing history of the samples. The results show that SHG is sensitive to the phase separation of the silicates bulk due to spinodal decomposition. A heuristic model based on Hf-O-Si polarizable units that explains the observed trends is presented.

# Table of Contents

# List of Tables

# List of Figures

# Chapter 1

# Introduction

## 1.1 Motivation

The study and understanding of surfaces and interfaces play an important role in modern science and technology. Powerful techniques have been devised to gain a deeper knowledge of these systems [1, 2]. However, many of such tools require measurements under ultrahigh vacuum (UHV) conditions; some others are invasive and can damage or contaminate the sample. Another limitation associated with many of the methods of surface science is their lack of access to buried interfaces.

Optical techniques don't suffer from some of the above mentioned problems. Particularly, they don't contaminate the sample, don't produce any damage if the fluence is kept under the damage threshold, can be used on most environments including UHV or high pressures, and have large penetration depth into condensed matter. On top of these, they can have micrometer lateral resolution, and femtosecond temporal resolution [3].

The large penetration depth of light into many materials allows optical techniques to access buried interfaces but the separation of interface and bulk signals is difficult and many times impossible. However, for centrosymmetric materials, in the dipole approximation, the bulk second order optical response vanishes identically due to symmetry. This cancelation leaves only the surface or

interface response, and higher order terms from the bulk to contribute to the observed signals [4–6]. The surface/interface signal sometimes can be separated from the bulk contribution based on symmetry arguments. Thus, when the separation can be carried out, second order optical processes offer a non-destructive, real time, *in situ*, and non-invasive surface specific diagnostic. Second order nonlinear processes include: Second Harmonic Generation (SHG), Sum Frequency Generation (SFG), Difference Frequency Generation (DFG), and optical rectification. When the top material layer is semitransparent to the exciting laser, and produced signal wavelengths, information about buried interfaces can be retrieved. Such characteristics have made these nonlinear processes into promising candidates to become a standard diagnostic for surfaces and interfaces. But more work is still necessary mainly in the description at microscopic level of the observed signals and its correlation with experimental observations. Of all the different second order processes, this work will focus on SHG measurements.

## 1.2 Historical perspective

In 1961 Franken and coworkers, using crystalline quartz, reported the first observation of optical frequency doubling opening the door for many other advances in nonlinear optics [7]. In the following year two seminal papers by Bloembergen and Pershan, dealing with the interaction of light with a nonlinear medium and the solution of Maxwell's equations in the boundary between nonlinear media, appeared [8, 9]. Also in 1962, SHG from surfaces of both centrosymmetric and non-centrosymmetric materials was observed by Lax, Mavroides and Edwards [10, 11]. In their paper they recognized that SHG in the centrosymmetric case could come from the surface breaking the symmetry. Other observations by dif-

ferent groups soon followed and at the same time they corroborated the existing theoretical predictions [12–16]. The first measurements of both magnitude and phase of $\chi^{(2)}$ were done in 1965 by Bloembergen, Chang and Ducuing [17].

On the theoretical side, progress was also made. Jha pointed out the importance of discontinuities in the normal component of the fundamental electric field to surface SHG contribution, and the existence of a bulk magnetic-dipole source [18, 19]. Shen and Bloembergen showed that bound electrons, and not only conduction electrons, contribute to frequency doubling in silver, and, together with Lee, that interband transitions are relevant for surface SHG [20, 21]. One year later Jha and Warke concluded that, far from resonance, the nonlinear polarization could be approximated in the long wavelength limit by the value of the dielectric function at the fundamental and second harmonic frequencies [22]. In 1968, as culmination of all the advances made, a paper reviewing the origin of the surface nonlinearity was published by Bloembergen, Chang, Jha and Lee [23].

In 1969 Wang performed experiments on liquid/air interfaces [24],and Brown and Matsuoka reported SHG sensitivity to surface adsorbates for the first time. This was in opposition to all previous theoretical and experimental work [25]. At that time surface preparation techniques were rather poor. This hindered the accurate test of theoretical predictions and was in part to blame for not recognizing the full value of second order nonlinear processes as surface specific techniques. Later Simon, Mitchell and Watson applied attenuated total reflection techniques, which enhance the response by coupling into surface plasmons or polaritons, to the production of second harmonic [26]. Rudnick and Ster considered the microscopic sources of SHG production at a metal surface [27]. In this paper the

authors found that the signal coming from breaking the inversion symmetry at a cubic metal surface was of the same order as the previously considered quadrupole arising from discontinuity of the normal component of the electric field. In 1976 Bower extended the above mentioned work by Jha to the case close to resonance and also included the effect of surface states [28].

Starting in the 80's, studies have focused less in the investigation of the nonlinear phenomenon in itself and more in the use of SHG as a surface analytical tool [29]. In a historical overview of the field of surface nonlinear optics Bloembergen points out that its history can be divided in three stages: "classical antiquity" referring to the initial development period of the sixties, "middle ages" for the seventies due to the somewhat little activity, and "renaissance" on the early eighties because of the renewed interest on the potential of the field [30]. This renaissance was in large part motivated by the observation by Chen, de Castro and Shen of an enhancement of the signal from a roughened surface [31]. With this new direction, the need of discriminating surface and bulk contributions became critical. Several authors worked on the problem, some relevant contributions were done by Guyot-Sionnest, Chen and Shen [32]; Sipe, Moss and van Driel [33]; and Sipe, Mizrahi and Stegeman [34]. In 1984 the first SHG study under UHV of a well characterized surface was published by Shen and coworkers [35]. Two years later, McGilp and Yeh obtained structural information of a buried metal-semiconductor interface using SHG [36].

A factor that contributed enormously to a wider use and development of nonlinear optical techniques was the invention of the mode-locked Titanium:Sapphire laser and of the tunable optical parametric amplifier/oscillator [37–39]. These

technologies are critical to SHG since the signal depends quadratically on the peak intensity of the fundamental light, Ultrashort pulses with very modest energy per pulse but high repetition rates allow high signal levels without damage to the sample due to excessive heating [40].

In more recent times, Second Harmonic Generation and Sum Frequency Generation have proved useful in the study of many different characteristics of the Si(001) and Si(111) surfaces, and the interface of the technologically relevant $Si/SiO_2$ system such as: strain [41–43], angstrom scale micro-roughness [44, 45], atomic adsorption of different elements [46–50], vibrational modes of adsorbates [51–53], vicinality [54, 55], surface phase transformation [56], phase transitions [57], interfacial dc electric field [58–60], charge trapping [61–65], temperature induced spectral shifts [66], sub-stoichiometric oxide formation [67], high-$\kappa$ dielectric layers [68, 69], etc. Although this list of properties that have been probed by SHG and SFG in Si is long, it must be recognized that these techniques still need to be better understood from a microscopic point of view in order to deliver on their promise of becoming a standard and commercially available tool for surface and interface diagnostics.

Currently the theory of surface nonlinear response is much less developed than the theory of the linear response. However the field has continued to grow and the understanding at the microscopic level is improving. Polarizable bond models and semi-empirical tight binding models make use of experimental data to adjust the value of different parameters while *ab initio* calculations are truly from first-principles. Both methods have been maturing in the last decade and several papers have been published with significant contributions to the field [50, 70–

80]. Second order nonlinear processes, in particular SHG, are closer to becoming standard surface/interface specific probes.

## 1.3 Second order nonlinear processes

In this section a brief phenomenological description of Second Harmonic Generation in reflection is given. Since most of these results are well known, emphasis will be made in the resulting expressions that describe the observed signal rather than in their detailed derivation. The system of interest in this work is the interface between Si(001) and $SiO_2$ or Hf-silicates. The goal of this section is to offer a compendium of results for SHG from the Si(001)/$SiO_2$/high-$\kappa$ dielectric system. For a more complete picture the reader is encouraged to refer to one of the several excellent review papers or textbooks that have been published on the subject [3–6, 29, 81–85]. The SHG signal produced by the dielectric films is negligible. Thus only contributions from the interfaces and from Si will be considered. All the derived equations will be specialized to the case of SHG in reflection from the Si(001) surface.

When a fundamental optical beam at frequency $\omega$ ($\boldsymbol{E}^{(\omega)}$) is incident in a material system it induces a polarization per unit volume $\boldsymbol{P}$. This polarization acts as a source of radiation in the nonlinear wave equation. If the intensity of the exciting laser is low, $\boldsymbol{P}$ can be modeled as a linear function of the incident electric field. However, if $\boldsymbol{E}^{(\omega)}$ is intense enough, the relation between the polarization and the incident optical field will no longer be linear. The lowest order correction is given by a term that depends quadratically in the field, *i.e.* second order optical nonlinearities of the material are being manifested. For SHG, assuming that $\boldsymbol{E}^{(\omega)}$

is proportional to $e^{i\omega t}$, the correction to the polarization will be proportional to $e^{i2\omega t}$. This source term will be represented by $\boldsymbol{P}^{(2\omega)}$ to emphasize its frequency dependence. So, the total polarization is given by:

$$\boldsymbol{P} = \underbrace{\chi^{(1)} \cdot \boldsymbol{E}^{(\omega)}}_{\text{Linear Term}} + \underbrace{\chi^{(2)} : \boldsymbol{E}^{(\omega)}\boldsymbol{E}^{(\omega)}}_{\boldsymbol{P}^{(2\omega)}}, \tag{1.1}$$

where $\chi^{(2)}$ is the second order nonlinear susceptibility which contains the nonlinear properties of the material under consideration.

The physical origin of $\boldsymbol{P}^{(2\omega)}$ is the "deformation" of the electronic distribution in the material due to the presence of $\boldsymbol{E}^{(\omega)}$. The details of this deformation will depend of the surroundings of the electrons. For example: the response of the electrons well inside the bulk of the material won't be the same as that of the electrons near the surface, or of those in areas where an external dc electric field is present.

It has been customary in the literature to separate the bulk and surface contributions into different susceptibility terms $\overleftrightarrow{\chi}^{(2),B}$, and $\overleftrightarrow{\chi}^{(2),S}$ respectively. Each of these terms is further decomposed into its multipolar expansion components. The bulk dipolar response is expected to dominate the SHG signal, followed by the surface dipole, the bulk electric quadrupole, and the bulk magnetic dipole. However, there is a very important exception to this rule, the case when the bulk atomic arrangement possesses a center of inversion (centrosymmetric materials). In this case symmetry imposes the restriction that the bulk dipolar term must be identically zero. The presence of the surface breaks the centrosymmetry and allows a dipolar response from the first few atomic layers of the material. Also, the normal component of $\boldsymbol{E}^{(\omega)}$ is discontinuous at the surface giving rise to a

surface quadrupolar response. These two contributions are grouped into the surface susceptibility $\overleftrightarrow{\chi}^{(2),S}$ which is expected to dominate the total signal for these materials, although the bulk electric quadrupolar susceptibility also contributes.

This work will focus on studying the SHG response from the interface between Si and $SiO_2$ or $Hf_{(1-x)}Si_xO_2$ (with $0 \leq x \leq 1$). For these systems, an important assumption will be made: the bulk of the oxides deposited on top of Si and their surface exposed to air have a negligible contribution to the measured SHG. This is a reasonable assumption that has been verified phenomenologically in both cases. The main contribution of these materials is through its interface with Si, and is accounted for by the effective surface susceptibility term.

Bulk silicon has a diamond lattice and therefore is centrosymmetric. Since on top of the dominant surface contribution to the SHG response, a weak bulk quadrupolar contribution is also observed, the total second order polarization vector can be written as:

$$P_i^{(2\omega)} = \chi_{ijk}^{(2),S} E_j^{(\omega)} E_k^{(\omega)} + \chi_{ijkl}^{(2),Q} E_j^{(\omega)} \nabla_k E_l^{(\omega)}. \tag{1.2}$$

In this equation the summation convention is assumed, *i.e.* repeated indices in the same side of the equation are summed over all possible values of that index. The suffix "$Q$" on the susceptibility refers to its quadrupolar bulk origin. Also note that $E^{(\omega)}$ refers to the fundamental electric field *inside* the material. A magnetic dipole term is nonexistent since Si is a non-magnetic material. As mentioned before, it is also possible to have other contributions from elements that break the bulk centrosymmetry, for example an applied dc electric field. These terms will be dealt with in subsequent chapters.

Bulk Si belongs to the m3m crystal class [86, 87]. In general 81 components are needed to fully describe a fourth rank tensor such as the bulk quadrupolar susceptibility tensor $\overleftrightarrow{\chi}^{(2),Q}$. However this number is reduced by the symmetries of the system. The bulk susceptibility of Si has 21 nonzero tensor components but only 3 of these are independent:

$$\begin{aligned}
&\chi^{(2),Q}_{XXXX} = \chi^{(2),Q}_{YYYY} = \chi^{(2),Q}_{ZZZZ} \\
&\chi^{(2),Q}_{XXYY} = \chi^{(2),Q}_{XXZZ} = \chi^{(2),Q}_{YYZZ} = \chi^{(2),Q}_{YYXX} = \chi^{(2),Q}_{ZZXX} = \chi^{(2),Q}_{ZZYY} = \\
&= \chi^{(2),Q}_{XYYX} = \chi^{(2),Q}_{XZZX} = \chi^{(2),Q}_{YZZY} = \chi^{(2),Q}_{YXXY} = \chi^{(2),Q}_{ZXXZ} = \chi^{(2),Q}_{ZYYZ} \\
&\chi^{(2),Q}_{XYXY} = \chi^{(2),Q}_{XZXZ} = \chi^{(2),Q}_{YZYZ} = \chi^{(2),Q}_{YXYX} = \chi^{(2),Q}_{ZXZX} = \chi^{(2),Q}_{ZYZY}.
\end{aligned} \tag{1.3}$$

Analogously, in the most general case 27 components are required to completely describe a third rank tensor such as $\overleftrightarrow{\chi}^{(2),S}$, but for the Si(001) surface (4m symmetry) only 7 elements are nonzero and of these only 3 are independent:

$$\begin{aligned}
&\chi^{(2),S}_{ZZZ} \\
&\chi^{(2),S}_{ZXX} = \chi^{(2),S}_{ZYY} \\
&\chi^{(2),S}_{XXZ} = \chi^{(2),S}_{YYZ} = \chi^{(2),S}_{XZX} = \chi^{(2),S}_{YZY}.
\end{aligned} \tag{1.4}$$

Up to this point the susceptibilities components have been implicitly assumed to be in the so called crystal reference frame. In the case of Si, the choice for such reference system is obvious due to the cubic symmetry of the crystal, namely the axes $(X, Y, Z)$ coincide with the crystallographic directions [100], [010], and [001] respectively. However, since it is more convenient to work in a reference frame tied to the laboratory, another set of coordinate axes is introduced called the laboratory frame $(x, y, z)$. This frame is given by coordinates such that $xy$

plane coincides with the Si surface, $xz$ plane coincides with the plane of incidence and, the $x$ axis is in the [110] direction. This implies that the $z$ axis will overlap with the crystallographic $Z$ axis. This choice of axis follows the work by Aktsipetrov and coworkers [87].

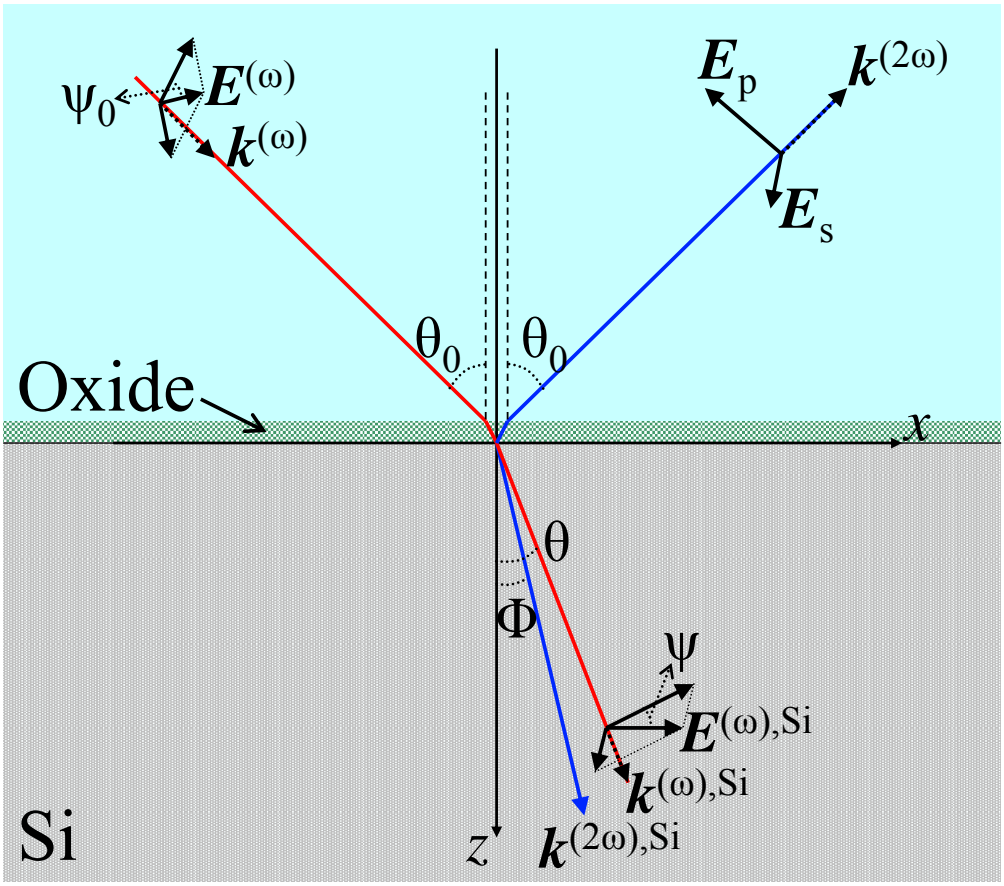


Figure 1.1: Geometry used for describing SHG in reflection. $\boldsymbol{E}^{(\omega)}$ and $\boldsymbol{E}^{(\omega),Si}$ are the pump fields in air and silicon respectively. $\psi_0$, and $\psi$ are the angles between the plane of incidence and the fundamental optical fields. $\boldsymbol{k}^{(2\omega),Si}$ is the wave vector of the transmitted SHG radiation.

Figure 1.1 shows the geometrical arrangement used to describe the SHG production. The incident fundamental field, $\boldsymbol{E}^{(\omega)}$, has an arbitrary linear polarization characterized by the angle $\psi_0$ with respect to the plane of incidence ($\psi_0 = 0°$

for p-polarized input; $\psi_0 = 90°$ for s-polarized input). The polarization state of the fundamental field transmitted into the Si substrate (described by angle $\psi$) can be determined using the linear Fresnel equations and Snell's law. This angle will be needed later to calculate the SHG contributions of the surface and bulk under rotations of the sample. The resulting expression after taking into account the presence of the oxide is:

$$\tan\psi = \tan\psi_0 \frac{\left(n_{Ox}^{(\omega)}\cos\theta + n_{Si}^{(\omega)}\cos\alpha\right)\left(\cos\alpha + n_{Ox}^{(\omega)}\cos\theta_0\right)}{\left(n_{Ox}^{(\omega)}\cos\alpha + n_{Si}^{(\omega)}\cos\theta\right)\left(\cos\theta_0 + n_{Ox}^{(\omega)}\cos\alpha\right)}; \qquad (1.5)$$

in this equation $n_{Ox}^{(\omega)}$ and $n_{Si}^{(\omega)}$ are the oxide and silicon refractive indexes at the fundamental wavelength. The angle of the fundamental field with the normal inside Si is given by $\sin\theta = \sin\theta_0/n_{Si}^{(\omega)}$, and the angle $\alpha$ between the fundamental and the normal inside the oxide is $\sin\alpha = \sin\theta_0/n_{Ox}^{(\omega)}$. Angle $\Phi$ can be determined using the nonlinear version of Snell's law, the result is $\sin\Phi = \sin\theta_0/n_{Si}^{(2\omega)}$.

Now it is necessary to write the equations that will determine the nonlinear polarization and from these expressions make a connection to the SHG field and measured intensity. Since the samples will be rotated around the $z$ axis by an angle $\phi$, the susceptibility tensors should be transformed accordingly using as many rotation matrices as the number of indices in the tensor. Once the rotated tensor components are obtained, they are introduced into Eq. (1.2) together with the expression for the cartesian coordinates, in the laboratory frame, of the fundamental field inside the Si substrate $\boldsymbol{E}^{(\omega),\,Si} = \left|E^{(\omega),\,Si}\right|(\cos\psi\cos\theta, \sin\psi, -\cos\psi\sin\theta)$. The magnitude of this vector can be obtained from $\left|\boldsymbol{E}^{(\omega)}\right|$ using the linear Fresnel coefficients from the incident medium $a$ to the transmitted medium $b$:

$$t_{\perp}^{a/b} = \frac{2n_a\cos\theta_a}{n_a\cos\theta_a + n_b\cos\theta_b}, \qquad t_{\parallel}^{a/b} = \frac{2n_a\cos\theta_a}{n_a\cos\theta_b + n_b\cos\theta_a}; \qquad (1.6)$$

$\theta$ is the angle of incidence in the corresponding medium. The result is:

$$\left|\boldsymbol{E}^{(\omega),\,Si}\right|^2 = \left(t_{\perp}^{Ox/Si} t_{\perp}^{Air/Ox} E^{(\omega)} \sin\psi_0\right)^2 + \left(t_{\parallel}^{Ox/Si} t_{\parallel}^{Air/Ox} E^{(\omega)} \cos\psi_0\right)^2 . \quad (1.7)$$

After some algebra, it turns out that there is no anisotropic response from the (001) surface, *i.e.* the results do not depend on the rotation angle $\phi$. The resulting isotropic p-polarized second order surface polarization is [87]:

$$\begin{aligned} P_{p,\,isot}^{(2\omega),\,S} &= \left|E^{(\omega),\,Si}\right|^2 \left\{-\chi_{xzx}^{(2),\,S} \sin 2\theta \cos^2\psi \cos\theta + \right. \quad (1.8)\\ &\quad \left. + \left[\left(\chi_{zzz}^{(2),\,S} \sin^2\theta + \chi_{zxx}^{(2),\,S} \cos^2\theta\right) \cos^2\psi + \chi_{zxx}^{(2),\,S} \sin^2\psi\right] \sin\theta \right\} ; \end{aligned}$$

while the isotropic s-polarized surface response is:

$$P_{s,\,isot}^{(2\omega),\,S} = \left|E^{(\omega),\,Si}\right|^2 \left(-\chi_{xzx}^{(2),\,S} \sin 2\psi \sin\theta\right) . \quad (1.9)$$

For the quadrupolar bulk response there are both isotropic and anisotropic contributions. The following expressions for the nonlinear polarization separate these contributions for future reference. The expressions for the isotropic quadrupolar bulk p-, and s-polarized SHG contributions are:

$$\begin{aligned} P_{p,\,isot}^{(2\omega),\,Q} &= \imath \left|E^{(\omega),\,Si}\right|^2 k^{(\omega),\,Si} \\ &\quad \left\{\left[\cos^2\psi \left(1/4 \sin\theta \cos^2\theta \left\{3\chi_{xxxx}^{(2),\,Q} - 6\chi_{xxyy}^{(2),\,Q} + \chi_{xyxy}^{(2),\,Q}\right\} + \sin^3\theta \chi_{xyxy}^{(2),\,Q}\right)\right.\right. \\ &\quad + 1/4 \sin^2\psi \sin\theta \left\{\chi_{xxxx}^{(2),\,Q} - 2\chi_{xxyy}^{(2),\,Q} + 3\chi_{xyxy}^{(2),\,Q}\right\}\Big] \cos\theta \quad (1.10)\\ &\quad + \left[\cos^2\psi \left(\chi_{xyxy}^{(2),\,Q} \cos^3\theta - \sin^2\theta \cos\theta \left\{\chi_{xxxx}^{(2),\,Q} - 2\chi_{xxyy}^{(2),\,Q}\right\}\right)\right. \\ &\quad \left.\left. + \chi_{xyxy}^{(2),\,Q} \cos\theta \sin^2\psi\right] \sin\theta \right\} \\ P_{s,\,isot}^{(2\omega),\,Q} &= \imath \left|E^{(\omega),\,Si}\right|^2 k^{(\omega),\,Si}\ 1/8 \sin 2\theta \sin 2\psi \left(\chi_{xxxx}^{(2),\,Q} - 2\chi_{xxyy}^{(2),\,Q} - \chi_{xyxy}^{(2),\,Q}\right) . \quad (1.11) \end{aligned}$$

For the anisotropic response of the quadrupolar bulk the expressions are:

$$\begin{aligned} P_{p,\,anis}^{(2\omega),\,Q} &= \imath \left|E^{(\omega),\,Si}\right|^2 k^{(\omega),\,Si}\; 1/4 \cos\theta \left\{ \left[\chi_{xxxx}^{(2),\,Q} - 2\chi_{xxyy}^{(2),\,Q} - \chi_{xyxy}^{(2),\,Q}\right] \right. \qquad (1.12) \\ &\quad \left. \times \left[\sin\theta \cos 4\phi \left(\cos^2\psi \cos^2\theta - \sin^2\psi\right) + \sin 2\theta \sin 2\psi \sin 4\phi\right] \right\} \\ P_{s,\,anis}^{(2\omega),\,Q} &= \imath \left|E^{(\omega),\,Si}\right|^2 k^{(\omega),\,Si}\; 1/4 \left(\chi_{xxxx}^{(2),\,Q} - 2\chi_{xxyy}^{(2),\,Q} - \chi_{xyxy}^{(2),\,Q}\right) \qquad (1.13) \\ &\quad \times \left[\sin\theta \sin 4\phi \left(\cos^2\psi \cos^2\theta - \sin^2\psi\right) - \sin 2\theta \sin 2\psi \cos 4\phi\right]. \end{aligned}$$

The total nonlinear polarization is obtained from adding the different contributions from these equations. A connection between $\boldsymbol{P}^{(2\omega)}$ and $\boldsymbol{E}^{(2\omega)}$ is established through the following expressions [9]:

$$\begin{aligned} E_{p-pol}^{(2\omega)} = & \\ & \frac{n_{Ox}(2\omega)\left\{n_{Si}^2(\omega)\left[n_{Si}^2(2\omega) - \sin^2\theta_0\right]^{1/2} - n_{Si}^2(2\omega)\left[n_{Si}^2(\omega) - \sin^2\theta_0\right]^{1/2}\right\}}{n_{Si}(\omega)\left\{n_{Si}^2(2\omega)\left[n_{Ox}^2(2\omega) - \sin^2\theta_0\right]^{1/2} + n_{Ox}^2(2\omega)\left[n_{Si}^2(2\omega) - \sin^2\theta_0\right]^{1/2}\right\}} \\ & \times \frac{4\pi P_{p-pol}^{(2\omega)}}{\left[n_{Si}^2(\omega) - n_{Si}^2(2\omega)\right]}, \end{aligned} \qquad (1.14)$$

$$\begin{aligned} E_{s-pol}^{(2\omega)} = & \\ & \frac{\left[n_{Si}^2(2\omega) - \sin^2\theta_0\right]^{1/2} - \left[n_{Si}^2(\omega) - \sin^2\theta_0\right]^{1/2}}{\left[n_{Ox}^2(2\omega) - \sin^2\theta_0\right]^{1/2} + \left[n_{Si}^2(2\omega) - \sin^2\theta_0\right]^{1/2}} \; \frac{4\pi P_{s-pol}^{(2\omega)}}{\left[n_{Si}^2(\omega) - n_{Si}^2(2\omega)\right]}. \end{aligned} \qquad (1.15)$$

Once the second harmonic fields are obtained, they just need to be substituted in the expression for the intensity $I_{p,s}^{(2\omega)} = \frac{c}{8\pi}\left|E_{p,s}^{(2\omega)}\right|^2$, which is what is actually measured in the laboratory.

## 1.4 Scope of this work

The main focus of this work is SHG spectroscopy. Of the several aspects of this technique that are still under active research, this work will focus on only two

of them: extending the bandwidth, and measuring the SHG phase. Also, results of an SHG study of the interface between Si and Hf-silicates will be presented to illustrate the potential of SHG as a *in-situ*, non-invasive technique. It will be shown that the amplitude is sensitive to different conditions of the sample's growth environment.

The SHG theory presented in the previous section assumed that both the fundamental beam and the nonlinear polarization were plane waves. Chapter 2 introduces the use of broad bandwidth pulses which break the plane wave assumption. An extension of the theory is given in order to include broad bandwidth pulses. Spectral data acquired using a Ti:Sapp oscillator capable of $\Delta\lambda > 100\,\mathrm{nm}$ is presented. At the end of the chapter a different approach to extend the spectral range is considered, namely SFG between the fundamental beam and a white light continuum (WLC) generated using photonic crystal fibers. Chapter 3 shows a SHG study of the technologically relevant $Si/SiO_2/Hf_{(1-x)}Si_xO_2$ structures, and a microscopic phenomenological model to explain the observed trends. Chapter 4 offers several examples of phase measurements using broad bandwidth pulses. These examples illustrate phase shifts in GaAs coming from the interference from bulk and surface SHG, time dependent phase shifts, and measurements of the complex value of the bulk and surface second order susceptibility from silicon. Chapter 5 states the conclusions and looks at possible future developments for SHG spectroscopy.

# Chapter 2

# Ultra-broad bandwidth SHG spectroscopy

The discussion and derivations presented in the previous chapter assumed that the fundamental and SHG fields were plane waves. These approximations work well for many scenarios where spectral information is obtained by tuning a narrow bandwidth ($\tau_p \geq 100\,\text{fs}$) laser. However, laser tuning is time consuming and prone to misalignments sacrificing real-time SHG data acquisition. One way to avoid the need for laser tuning is to use pulses with durations well below 100 fs. Such pulses naturally have broad frequency bandwidths, for example a $\tau_p$ =10 fs transform limited Gaussian pulse centered at $\lambda$ =800 nm has a spectral bandwidth of $\Delta\lambda$ =94 nm measured at full width at half maximum (FWHM). This is because the relation $\Delta\omega\tau_p \geq 2.77$ between frequency and time domain descriptions must be obeyed.

The advantages that ultrashort pulses offer for SHG spectroscopy go beyond the broader spectral bandwidth. Unamplified oscillator pulses deposit modest amounts of energy in extremely short periods of time resulting in the high peak powers needed for exciting optical nonlinearities with low sample heating [40]. These sources are particularly attractive for $Si/SiO_2$ and Si/high-$\kappa$ dielectric studies because the resulting SH covers the $E_1$ silicon resonance region [88]. However when using large bandwidths, pulse chirp can induce spectral artifacts. The first part of this chapter will analyze the influence of such effects, how to handle

them, and also will present some results obtained using ultra-broad bandwidth pulses ($\approx 105\,\mathrm{nm}$ FWHM fundamental) directly from a Ti:Sapp oscillator.

A different approach to extending the spectral range is the use of white light continuum (WLC) generation. In principle a SHG signal could be obtained using WLC as the light source, but this scheme is very inefficient because of the low peak power of the incident light (due to chirp) and the $[I^{(\omega)}]^2$ dependence of the signal. Another way to use WLC is combining it with the fundamental pulse through self-dispersed sum frequency generation (SFG) [89]. In this scheme signal depends only linearly on the WLC intensity. As part of this work this technique was implemented in an attempt to extend the bandwidth but found only partial success. The WLC generation process, results obtained, and a discussion of the challenges found in the implementation are described in the final section.

## 2.1 Theory of SHG with broad bandwidth pulses

In this section some theoretical considerations related to the use of broad bandwidth pulses in SHG are studied. Understanding the assumptions involved in the description of the material response to ultrashort pulses will clarify the limitations of the technique.

Like all electromagnetic phenomena, a study of SHG from broad bandwidth pulses must begin with Maxwell's equations. From these equations a wave equation for the total electric field, $\boldsymbol{E}$, can be derived in the usual way, resulting in:

$$\left[\nabla \times (\nabla \times) + \frac{1}{c^2}\frac{\partial^2}{\partial t^2}\right] \boldsymbol{E}(\boldsymbol{r}, t) = -\frac{4\pi}{c^2}\frac{\partial^2}{\partial t^2}\boldsymbol{P}(\boldsymbol{r}, t). \tag{2.1}$$

In principle any linear or nonlinear optical process is fully characterized if

the polarization term is known since this would allow equation 2.1 to be solved. However it seldom happens that one has access to the precise form of this term. As in the previous chapter, all the multipolar contributions higher than the electric dipole term will be neglected. This approximation makes $\boldsymbol{P}$ a local function of $\boldsymbol{E}$. Within this restriction, the polarization vector is modeled, as pointed out before, by expanding it in a power series in terms of the electric field. The resulting expression in the time domain is:

$$\begin{aligned}\boldsymbol{P}(\boldsymbol{r},t) &= \int_{-\infty}^{t}\int_{-\infty}^{\infty}\chi^{(1)}(\boldsymbol{r}-\boldsymbol{r}',t-t')\cdot\boldsymbol{E}(\boldsymbol{r}',t')\mathrm{d}\boldsymbol{r}'\mathrm{d}t' \\ &\quad+\int_{-\infty}^{t}\int_{-\infty}^{t}\int_{-\infty}^{\infty}\int_{-\infty}^{\infty}\chi^{(2)}(\boldsymbol{r}-\boldsymbol{r}_1,t-t_1,\boldsymbol{r}-\boldsymbol{r}_2,t-t_2): \\ &\qquad\qquad\boldsymbol{E}(\boldsymbol{r}_1,t_1)\boldsymbol{E}(\boldsymbol{r}_2,t_2)\mathrm{d}\boldsymbol{r}_1\mathrm{d}\boldsymbol{r}_2\mathrm{d}t_1\mathrm{d}t_2 \\ &\quad+\cdots.\end{aligned} \tag{2.2}$$

In the plane wave approximation a monochromatic wave, and instantaneous material response are assumed at this point to simplify the time integral and obtain the first term on the right hand side of Eq. (1.2). But these assumptions can not be applied because of the broad bandwidth of the pulses, and the fact that material response times are of the same order of magnitude as the exciting pulses [90]. To move forward with the integration it must be realized that the surface dipolar response, coming from breaking the material bulk centrosymmetry, is restricted to a few atomic monolayers and can be modeled with a spatial delta function, *i.e.* $\chi^{(2)} \propto \delta(\boldsymbol{r}-\boldsymbol{r}_1)\delta(\boldsymbol{r}-\boldsymbol{r}_2)$.

For the time dependence a change of variables ($t-t_2=\tau_2$ and $t_2-t_1=\tau_1$)is performed, the fields are written in terms of their Fourier transforms on $\Omega$ and $\Omega'$ and finally the resulting expression is Fourier transformed to the frequency

domain leading to the following form of the nonlinear polarization for each tensor component of $\overleftrightarrow{\chi}$:

$$P^{(2\omega)} = \frac{1}{(2\pi)^2}\int_{-\infty}^{\infty}\chi^{(2)}(2\omega,\Omega,2\omega-\Omega)E(\Omega)E(2\omega-\Omega)\mathrm{d}\Omega; \tag{2.3}$$

where:

$$\chi^{(2)}(2\omega,\Omega,2\omega-\Omega) = \int_0^{\infty}\int_0^{\infty}\chi^{(2)}(\tau_2+\tau_1,\tau_2)e^{-i2\omega\tau_2}e^{-i\Omega\tau_1}\mathrm{d}\tau_2\mathrm{d}\tau_1. \tag{2.4}$$

Note that in Eq. (2.3) the fundamental electric field is convolved with the material properties contained in $\chi^{(2)}$. Therefore in general any distortion in the fundamental pulse, such as chirp, affects the measured spectral features and the material information can not be isolated.

For the case where there are no resonant frequencies of the material near the fundamental laser frequency, Eq. (2.3) can be further simplified to [91]:

$$P^{(2\omega)} = \frac{1}{(2\pi)^2}\chi^{(2)}(2\omega)\int_{-\infty}^{\infty}E(\Omega)E(2\omega-\Omega)\mathrm{d}\Omega. \tag{2.5}$$

All the material response is now outside of the integral, which depends only on features of the fundamental electric field that can be normalized out by an independent measurement on a spectrally flat material such as quartz. Obviously any interesting system will have some resonances that will impact the normalized spectra to some degree.

In order to quantify the influence of weak one-photon resonances on the normalization of measured spectra a model for the material is necessary. Miller found that for many materials it is possible to write the second order susceptibility as $\chi^{(2)}(2\omega,\Omega,2\omega-\Omega) = \Delta_m\chi^{(1)}(2\omega)\chi^{(1)}(\Omega)\chi^{(1)}(2\omega-\Omega)$ with $\chi^{(1)}$ being the linear susceptibility and $\Delta_m$ an almost constant coefficient [92]. Strictly speaking these

susceptibilities should be the surface susceptibilities but, as a first approximation, they can be substituted by the bulk susceptibilities. The incident fundamental pulses will be assumed to be Gaussian and given in the frequency domain by $E(\Omega) = E_0 e^{-(\Omega-\omega_l)^2/\sigma^2} e^{-\imath(\Omega-\omega_l)^2\phi''(\omega_l)/2}$ where the central frequency $\omega_l$ was chosen to cancel the first derivative of the phase $\phi'$. If these two assumptions are inserted in Eq. (2.3) and the fundamental frequency is rewritten as $\Omega = \omega + \delta$, with $\delta \ll \omega$, the result is [93]:

$$P^{(2\omega)} = e^{2\imath\phi(\omega)} \frac{\sigma \Delta_m \left|E(\omega)\right|^2}{(2\pi)^2} \sqrt{\frac{\pi}{2(1+\imath a)}} \chi^{(1)}(2\omega) Z(\omega) \left[1 + \frac{\sigma^2}{8(1+\imath a)} \frac{Z''(\omega)}{Z(\omega)}\right]; \tag{2.6}$$

with $Z(\Omega) = \chi^{(1)}(\Omega)\chi^{(1)}(2\omega - \Omega)$, and $a = \sigma^2\phi''/2$ a dimensionless chirp parameter.

The one-photon resonance of the material enters in 2 places in Eq. (2.6). First it enters as an overall multiplicative factor that will affect the measured spectra even in cases of narrow bandwidth pulses or broad bandwidth pulses with no chirp ($a = 0$). Second, it enters in the chirp-dependent factor inside the square brackets. To make a numerical evaluation of the effect of this last contribution, it is easier to write this expression using the refractive index of the material and its derivatives because they are tabulated, for example in Ref. [94]:

$$\frac{\sigma^2}{8(1+\imath a)} \frac{Z''(\omega)}{Z(\omega)} = \frac{(\Delta\lambda)^2}{1+\imath a} \frac{n^2}{2(n^2-1)} \left[\frac{n''}{n} + \frac{2n'}{\lambda n} + \frac{3n^2-1}{n^2-1}\left(\frac{n'}{n}\right)^2\right]. \tag{2.7}$$

Current Ti:Sapp technology is capable of bandwidths as wide as 700 nm at full width [95, 96]. This amazing characteristic involves a very careful compensation of higher order dispersion by using specially designed negatively chirped mirrors, and $CaF_2$ intracavity prisms. However most commercial and home-built

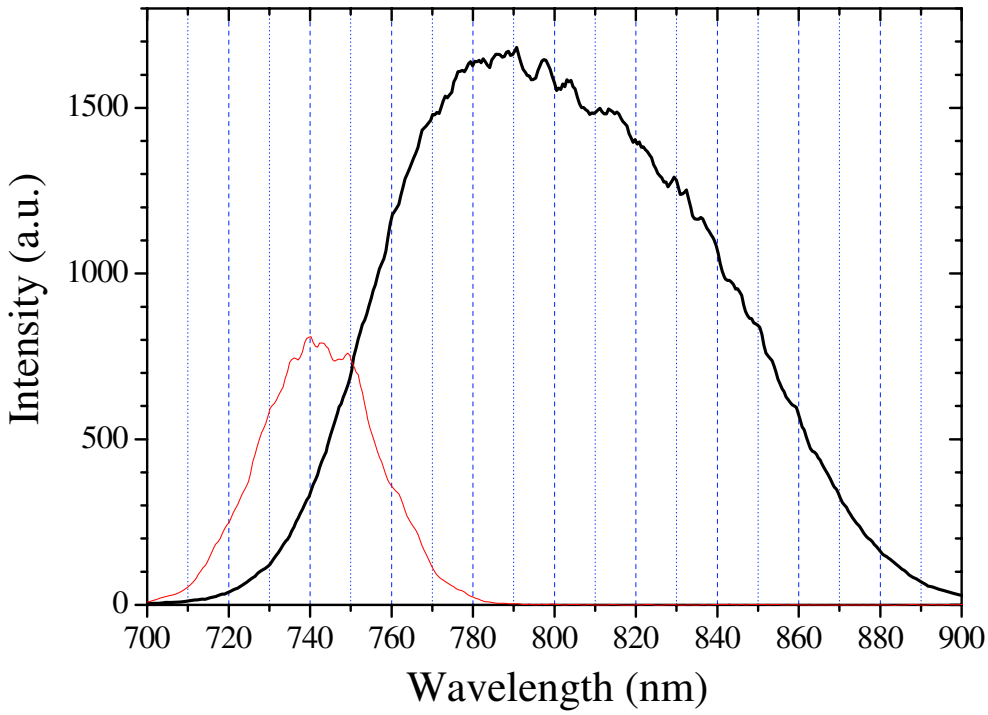


Figure 2.1: Laser spectra using standard blue optics set (red line) and ultra-broad bandwidth optics set (black line). The FWHM bandwidth is more than 100 nm in the later case. Average laser power is 500 mW and pulse duration approximately 10 fs.

oscillators have much narrower bandwidths. Figure 2.1 shows the spectrum of a typical Ti:Sapp oscillator (in red) with $\approx 33$ nm FWHM bandwidth resulting in $\approx 29$ fs pulses. For this conditions formula 2.7 gives a correction smaller than $10^{-3}$ for the case of Si. Thus spectra acquired with this laser should not suffer distortions due to the presence of one-photon resonances after normalization using a flat reference. Although the pulse characteristics of this laser are outstanding, shorter pulses can be obtained using off-the-shelf mirrors with special dielectric coatings but keeping the same fused silica intracavity prisms. A bandwidth of $\Delta\lambda = 100$ nm FWHM can be obtained in this new configuration as shown by the

black spectrum in Fig. 2.1. For such broad bandwidth the predicted influence of fundamental resonances of Si in the spectrum is less than $10^{-2}$.

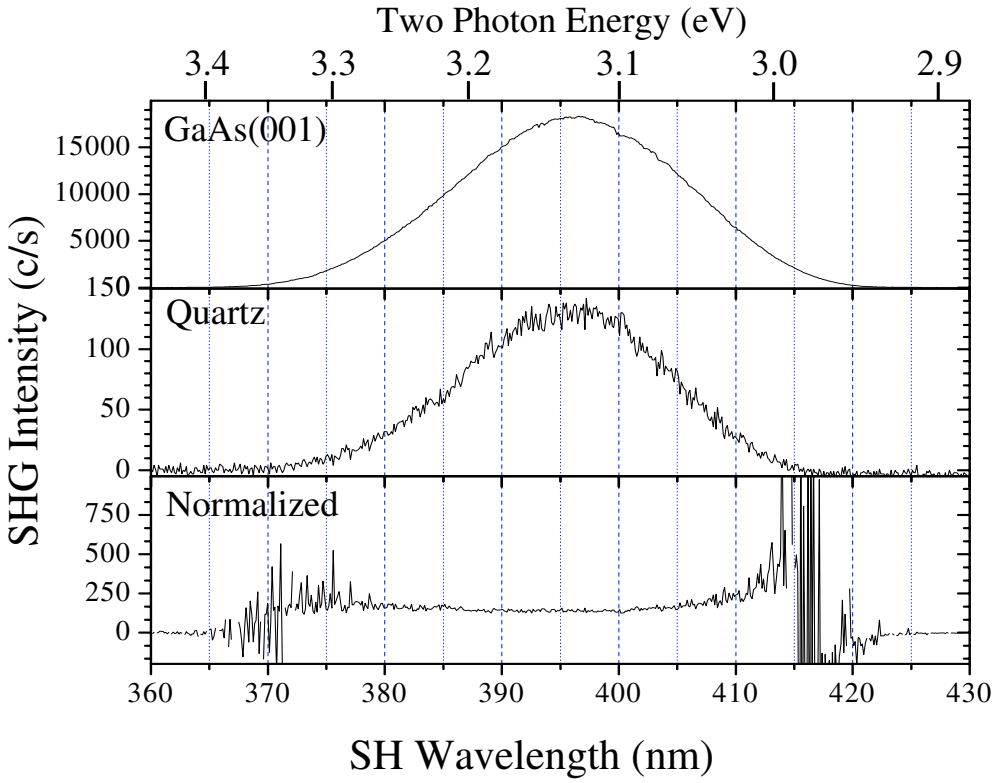


Figure 2.2: Top panel: GaAs(001) SHG spectrum taken with laser on broad bandwidth configuration. Middle panel: Quartz spectrum used for normalization. Bottom panel: Normalized GaAs SHG spectrum, noise is mainly due to the weak signal from the wings of quartz spectrum. All data taken on P-in/S-out polarization combination.

Figure 2.2 illustrates the normalization procedure for the case of GaAs. The top panel shows the SHG spectrum as recorded by the spectrometer CCD camera. The middle panel displays the quartz SHG spectrum. The lower panel contains the normalized GaAs spectrum. The noise at the edges of the spectrum is due to the weak quartz signal at the wings. The signal to noise ratio could be improved by longer exposure times. For a 100 nm FWHM fundamental transform

limited Gaussian pulse centered at 800 nm, a 36 nm FWHM SHG spectrum is expected. As the top panel of the figure shows the measured FWHM is approximately 25 nm. This reduction in bandwidth could be due to pulse stretching.

The normalized spectrum (see bottom panel) is almost featureless except for a weak increase in the signal towards the edge of the long wavelength wing. This feature is weak and noisy and a further bandwidth extension to longer wavelengths will be necessary to clarify if this is the onset of a resonant feature. The oxidized surface of GaAs(001) has a one photon resonance at approximately 1.45 eV (2.9 eV two photon energy) [97]. Some other examples of broad bandwidth spectroscopy and its comparison with narrow bandwidth spectroscopy can be found in Ref. [93].

## 2.2 SFG using white light continuum

As mentioned at the beginning of this chapter sum frequency generation (SFG) between fundamental and white light continuum (WLC) was used as an alternative approach to extend the spectral bandwidth of the measurements. The fixed wavelength fundamental beam is split and one part is used for the SFG process while the other is for WLC generation. A disadvantage of this approach is that WLC production from solid targets requires the use of amplified sources therefore increasing the laser system complexity. This last point was resolved by the use of a novel microstructure fiber for the WLC as explained below.

The principle of the SFG scheme is illustrated in the top left panel of Fig. 2.3. As mentioned before, the fundamental beam is split in two parts, the one labeled 800 nm in the figure goes through a delay arm and the other part is

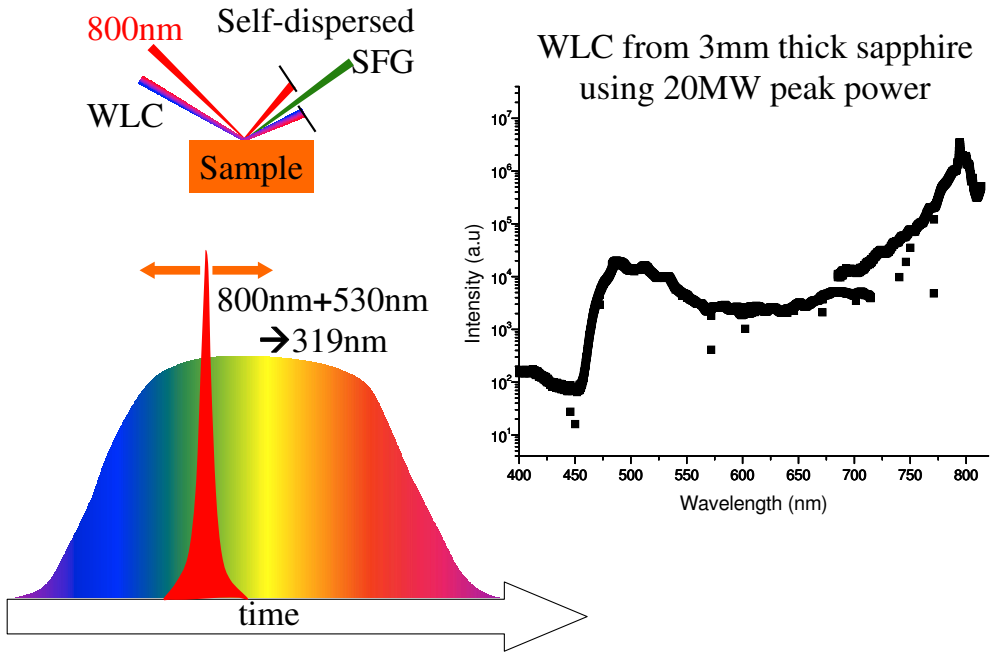


Figure 2.3: Illustration of the self dispersed WLC+800 nm SFG concept. Top left panel: schematic representation of different beams. Bottom left panel: representation of the overlap of green light (530 nm) from linearly chirped WLC with 800 nm fundamental to produce 319 nm SFG signal. Right panel: measured WLC generated from a 3 mm thick sapphire window using an amplified laser source.

used to generate the WLC light. This two beams are focused into the sample where they spatially overlap, the delay arm is used to also obtain a temporal overlap. When they strike the sample a SFG signal is produced. Momentum conservation along the surface for the produced photons requires that different SFG frequencies emanate from the surface at different angles with respect to the normal, this is called self-dispersing SFG [89]. If the WLC pulse duration is similar to that of the fundamental, all the frequencies in the continuum will be mixed with the 800 nm light and all the produced SFG frequencies will be spatially separated due to the self-dispersion. A linear detector or a CCD camera can be used to record a full spectrum in a few seconds.

The dispersion of the SFG signal is determined by the incident geometry. The angle of incidence (defined with respect to the normal to the surface) was 42° for the WLC and 48° for the 800 nm beam. This meant that for a continuum expanding from 400 nm to 1200 nm, the angular dispersion of the SFG signal would be 1.5°. If a CCD with 1100 pixels, each of them 24 $\mu$m long for a total detector length of 26.4 mm, is used it has to be placed 1 m away to completely fill the active area of the detector. The expected spectral resolution is approximately 0.2 nm/pixel.

The previous description corresponded to an ideal experiment, however the WLC pulse is actually several picoseconds long and chirped. The 800 nm pulse was around 100 fs long. In this case, instead of using the self-dispersing technique, the length of the delay arm could be varied so that different frequencies of the WLC were mixed with the fundamental for different delays. This idea is schematically shown in the lower left panel of Fig. 2.3. If the generated continuum is not linearly chirped, knowledge of the chirp structure is necessary to calibrate the produced SFG wavelength against the delay of the fundamental beam. This technique will sacrifice the real-time data acquisition capabilities of the system but the potential gain in terms of spectral range is significant. The advantages over laser tuning are that the fundamental laser source doesn't have to be tuned, only a delay line is required to mix different WLC colors with the fundamental, and the significantly wider bandwidth.

White light continuum (WLC) generation is caused by the process of self phase modulation (SPM) induced by the nonlinear index of refraction of the medium. When an intense laser beam is propagating in a material, it can modify

the material linear index of refraction ($n_0$) according to: $n = n_0 + n_2 I$ where $n_2$ is particular to each material and related to $\chi^{(3)}$ by the expression $n_2 = \frac{12\pi^2}{n_0^2 c}\chi^{(3)}$ [5]. If the pulse has a time profile given by $I(t)$, it will acquire a time dependent phase factor due to SPM of $\phi_{SPM}(t) = n_2 I(t)\omega_0 L/c$ when propagating through a medium with thickness $L$. The instantaneous frequency of this pulse is defined as:

$$\omega(t) = \omega_0 + \frac{\mathrm{d}}{\mathrm{d}t}\phi_{SPM}(t). \tag{2.8}$$

From this expression it is obvious that new frequency components will be created. For $n_2 > 0$ new low frequency components appear in the leading edge and new high frequencies in the trailing edge of the pulse. Although SPM is not a dispersive process in itself, the medium in which the new spectral components are propagating is dispersive and therefore the pulse will be chirped.

The first attempt to generate a WLC was done in a jet of water and glycol using amplified laser pulses with an energy of $\mu$J/pulse and a pulse duration of 150 fs. This scheme turned out to be inconvenient due to the use of liquids and because the generated continuum presented large intensity fluctuations. The jet was replaced by a 3 mm thick sapphire window that produced the spectrum shown on the right hand side of Fig. 2.3. As can be seen, the spectrum presented more than four orders of magnitude variations in intensity across the spectral range. The main peak was located at the same spectral position as the pump beam. Also the recorded spectrum was not always reproducible perhaps due to variations in the laser mode or temporal profile.

At the time of these experiments optical fibers based on photonic band gaps instead of total internal reflection were introduced [98–101]. These advances led

to the generation of an ultra-broad bandwidth WLC using a microstructure fiber [102]. The characteristics of this continuum are remarkable and well suited for this work, so the decision was taken to adapt this technology to SFG experiments. The major change in the setup was that this fibers do not require an amplified pump, a few nJ/pulse are enough for efficient WLC generation. The next few paragraphs will be devoted to describing the fiber and its properties.

The principle of operation for most optical fibers is total internal reflection (TIR). This effect exploits an index of refraction difference between the fiber core and cladding. In standard step-index fibers both elements are made of fused silica but the core is doped with $GeO_2$ to increase its index of refraction by approximately 2%. Even though fused silica has a very low nonlinear susceptibility, optical fibers made with it are efficient nonlinear media. This is because they can confine light in diameters of a few microns for very long interaction lengths. However short pulses can not propagate without broadening through regular fibers because the fiber group velocity dispersion (GVD) stretches the pulse during propagation increasing its temporal duration.

In any fiber there are two contributions to its total GVD, material dispersion (for bulk silica the GVD goes to zero around 1300 nm and below this wavelength it is negative), and waveguide dispersion. This last source arises because at longer wavelengths the propagating light is less confined by the higher index core and expands further into the lower index cladding, lowering the effective index of the guided mode. The waveguide contribution is usually negative (normal dispersion) and thus there are no conventional step-index fibers that have a zero-GVD wavelength below that of bulk silica. As a rule of thumb, for step

index fibers, the higher the core-cladding index contrast and the smaller the core size, the larger the waveguide contribution. Therefore the total GVD of a fiber can be modified to some degree by changing the core or cladding materials, or its geometrical characteristics.

A new type of fiber with GVD properties dramatically different from those of conventional fibers is obtained by drawing a solid fuse silica rod surrounded by hollow rods in a hexagonal closed packed arrangement. They are called microstructure fibers, holey fibers, or photonic crystal fibers. The resulting structure is illustrated in the microphotograph shown in the top left panel of Fig. 2.4 taken from Ref. [103]. The pure silica core is approximately 1.7 $\mu$m in diameter, and the surrounding air holes are 1.3 $\mu$m. Many other designs are possible and have been tried [104] but the one shown is what was used for the experiments.

Simulations show that this type of structure is closely equivalent to a high index contrast (silica/air) fiber when the air-filled fraction of the cladding is greater than approximately 60%. The index contrast is approximately 0.45 and light is guided by total internal reflection. It has been demonstrated that only the air holes closest to the core are necessary for light confinement and essentially the same continuum generating properties have been obtained using a tapered fiber with a diameter of 2$\mu$m [105].

This fiber has outstanding nonlinear properties because its zero-GVD point shifted to 767 nm allowing the propagation of ultrashort Ti:Sapp pulses without any significant dispersion for very long interaction lengths. An example of the WLC generation capabilities are illustrated in Fig. 2.4 where a picture of the dispersed continuum and its spectrum are shown. Note that, in contrast to the

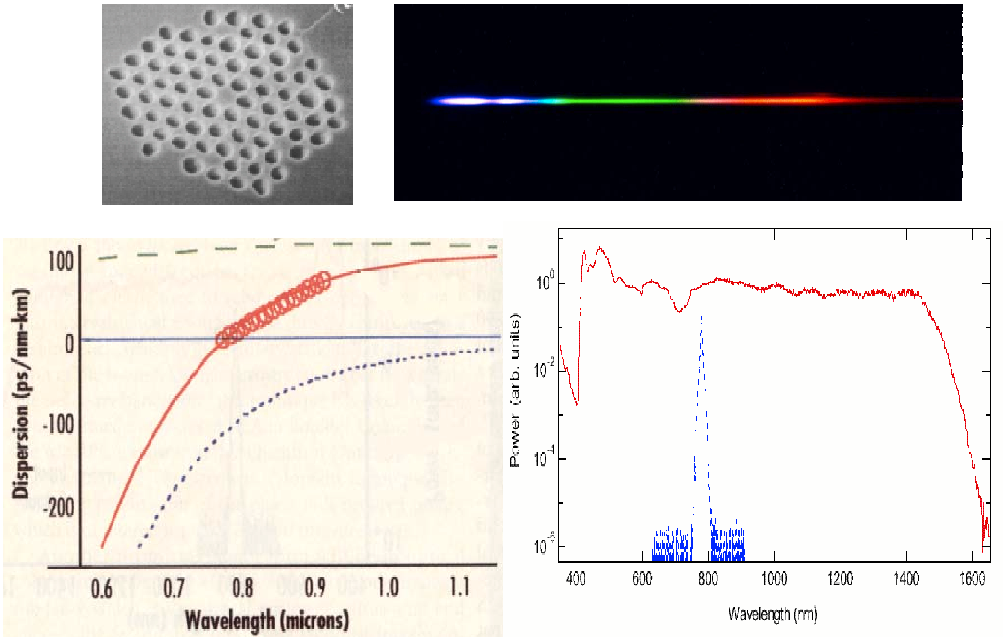


Figure 2.4: Some details of the microstructure fiber used in SFG experiments. Top left: microphotograph of fiber profile (core diameter is 1.7 $\mu$m, air holes diameter is 1.3 $\mu$m). Bottom left: net GVD of the fiber (solid red curve) and its contributions, waveguide GVD (dashed green curve) and material dispersion (dotted blue curve). Right panels: output spectrum generated using 100 fs pulses propagating through 75 cm of fiber. Blue line represents input pulse spectrum. All figures taken from reference [103]

sapphire generated WLC, the spectrum is very flat and does not present the same high peak at the pump wavelength. These spectral characteristics are even more impressive because the fundamental pulses were unamplified 100 fs with an energy of only 800 pJ/pulse.

The shifted zero-GVD point is the result of a dramatic shift in the waveguide GVD contribution. The lower left panel in Fig. 2.4, taken from Ref. [103], plots the fused silica material contribution to the total GVD in a dotted blue curve, the waveguide contribution in a dashed blue line, and the total fiber GVD in red.

The red circles represent measured values. The silica contribution is the same as in conventional fibers but the waveguide now exhibits anomalous dispersion well below 1300 nm. The sum of these two parts gives a fiber with normal dispersion below 767 nm but anomalous dispersion at higher wavelengths.

In this work the WLC used for SFG experiments was produced using 36 cm of microstructure fiber. Pulses from a Ti:Sapp oscillator with 30 fs duration, centered at 810 nm, and with an average power of 60 mW were coupled into the fiber using a 40× microscope objective. The output from the fiber had a large angular divergence close to 22° giving a numerical aperture of 0.36 and f/#=1.4. This represents a problem for the collimation optics at the output side. A microscope objective was used as an starting point but it had severe chromatic aberrations. The second approach was to use a spherical mirror with a focal length of 1 inch. The mirror worked better than the objective but since it had to be used in an off-axis configuration it induced astigmatism in the beam. The options of using a parabolic or elliptical mirror were also considered but it was not possible to find an off-the-shelf optic with the required f/#.

The broad bandwidth also presented a challenge in the detection arm because the short wavelengths of the WLC overlapped with the long wavelengths of the SFG signal. In principle the signal and WLC beam are spatially separated and this problem should be minimum; however in practice the scattering of the WLC by mirrors and sample was strong enough as to compete with the SFG signal. To solve this problem a suitable wide bandpass glass filter combination was used. It was found that the combination with the best rejection ratio was given by a RG750 filter before the sample to select long WLC wavelengths, and a BG39

filter in front of the detection to block these long wavelengths while allowing the shorter signal wavelengths to pass.

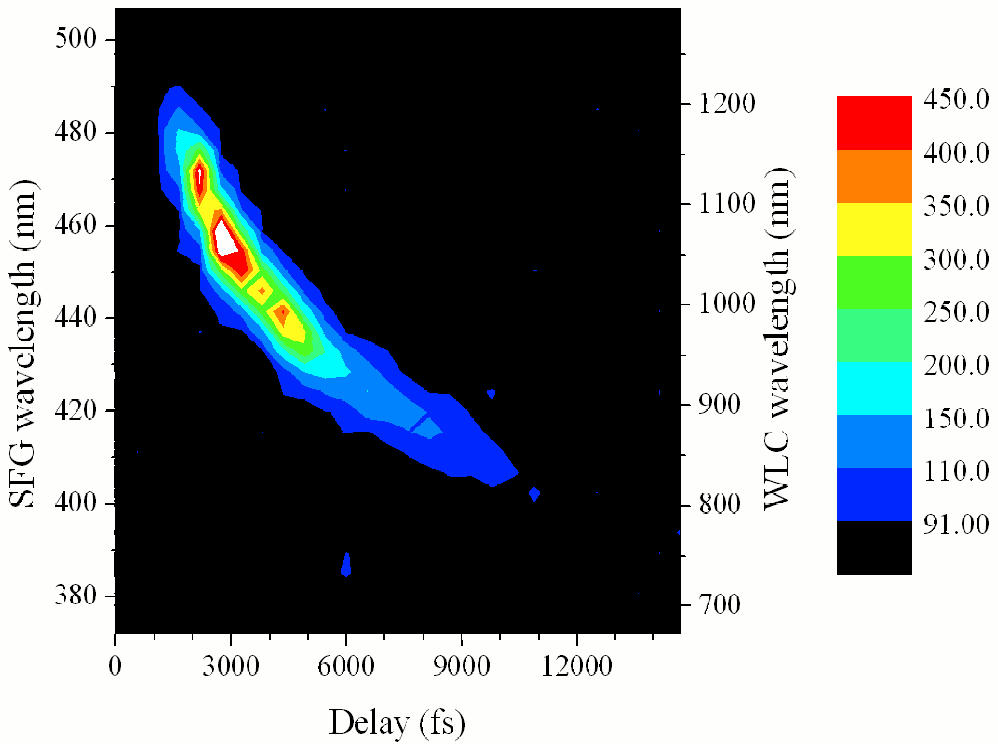


Figure 2.5: SFG signal from GaAs(001). Not all the WLC available bandwidth was used, only wavelengths higher than 800 nm.

Figure 2.5 shows the measured SFG signal from GaAs(001) using the filter combination described above. As can be seen from this plot, the WLC chirp is not linear and the pulse duration is close to 9 ps with the most intense part being approximately 5 ps long. These values are in the same order of magnitude as pulse duration measured by XFROG [106]. Several normalization attempts were made but it was not possible to find a spectrally flat standard that would produce strong SFG signals. The signal from quartz was essentially in the noise level. Roughened silver surfaces were also tried but no reliable normalization scheme

could be found. As discussed in the previous section normalization is paramount to get rid of spectral artifacts induced by the pulse chirp.

Experiments with Si were also tried but the signal was too weak. The strong chirp and long pulse duration are the reason for the weak observed signal levels. The natural next step was trying to compress the WLC to increase the peak power. A prism pair compressor was designed for this purpose. Simulations showed that the best option was to use SF10 prisms with a separation of approximately 45 cm. The compressor was built but major problems arose due to the long propagation distance, the poor beam collimation, and the astigmatism induced by the curved mirror.

In conclusion, it was possible to obtain broad bandwidth spectra from GaAs(001) using SFG; however no effective normalization scheme could be found that would work with such large bandwidths. The strong chirp of the WLC was used to tune to different wavelengths by changing the delay between the pulses. Recent literature suggests that using only a few mm of fiber is enough to generate a robust continuum without such strong chirp [107]. In future experiments this could be tried to generate either SHG or SFG signals, the SHG signal will benefit the most since it depends quadratically on the WLC intensity. Yet another approach to bandwidth extension for spectroscopy involves using a recently developed noncollinear optical parametric amplifier (NOPA) which can generate few fs pulses tunable across all the visible spectrum [108, 109].

# Chapter 3

# SHG study of high-$\kappa$ dielectrics on Si

Due to their architectural simplicity, and high performance, metal-oxide-semiconductor (MOS) structures have been at the heart of the microelectronics revolution. Since defects in the substrate or isolator layer of MOS structures can act as charge traps, device reliability and performance are intimately related to the density of defects of the chosen materials. While it is possible to grow crystalline semiconductors with very low defect densities, it is very difficult to control the quality of their interfaces with the oxide. There are several reasons why the $Si/SiO_2$ system has been the industry choice for MOS construction: thermodynamical and chemical stability, oxide dielectric constant ($\kappa = 3.9$), low density of bulk fixed charge, but mainly for its exceptionally high interface quality (interfacial trap densities $\approx 10^{10}\,\mathrm{cm}^{-2}$).

As the minimum device feature decreases, ultrathin insulator layers present new challenges including, but not limited to, dopant migration, and tunneling currents. Dopant migration can be successfully dealt with by the incorporation of nitrogen in the growth process to form $SiO_xN_y$ [110, 111]. The substitution of $SiO_2$ by a high-$\kappa$ material constitutes the most promising approach to reduce the tunneling leakage current to acceptable levels ($< 1\,\mathrm{A/cm}^2$ at $\sim 1\,\mathrm{V}$) while maintaining the same capacitance [112]. The advantage of using a material with

higher $\kappa$ can be seen from the following equation for a parallel plate capacitor:

$$C = \kappa\epsilon_0 \frac{A}{d}; \tag{3.1}$$

where $A$ is the area of the electrodes, and $d$ the dielectric thickness. If $C$ is to remain constant and $\kappa$ is increased, then $d$ must increase too. Thus high-$\kappa$ materials allow the use of a thicker insulator layer, which in turn means a higher barrier against diffusion and tunneling leakage currents.

Selecting a suitable replacement candidate for $SiO_2$ involves many different factors like: chemical and thermodynamical stability, electrical properties, compatibility with production line processes, film morphology, reliability, etc. [113]. Some examples of high-$\kappa$ materials are: $Al_2O_3$, $Ta_2O_5$, $TiO_2$, $Y_2O_3$, $CeO_2$, $ZrO_2$, and $HfO_2$. Another problem that arises for high-$\kappa$ oxides is the phenomenologically observed trend that as the dielectric constant increases, the band gap of the material decreases. This results in lower conduction and valence band offsets with Si which increase conduction through the interface due to carriers injected into the bands of the oxide. This leakage is acceptable if the band offsets are greater than 1 eV. Taking all these factors into consideration, thus far $HfO_2$ and Hf-silicates have emerged as the leading replacement candidates [114].

$SiO_2$ has $\kappa \approx 3.9$ while $HfO_2$ has $\kappa \approx 25$, thus a gate oxide made of $HfO_2$ with a thickness of $\approx 65$ Å results in the same capacitance as a $SiO_2$ gate of only $\approx 10$ Å [see Eq. (3.1)]. For Hf-silicates [$Hf_{(1-x)}Si_xO_2$] the dielectric constant and the band offsets depend on Si content; $\kappa$ varies from 25 for $x = 0$ to 8 for $x = 0.65$. The silicate conduction band offset does not change with $x$ but the valence band offset goes from 4.4 eV ($x$=1) to 3.4 eV ($x$=0.6) as illustrated on Fig. 3.1(b). Even though $\kappa$ and valence band offset for silicates are lower than for $HfO_2$, they are

attractive because their defect density can also be much lower [115, 116]. Another advantage of silicates vs. pure oxide is that the crystallization temperature increases with alloying. This is important to minimize leakage currents through grain boundaries of polycrystalline structures [117].

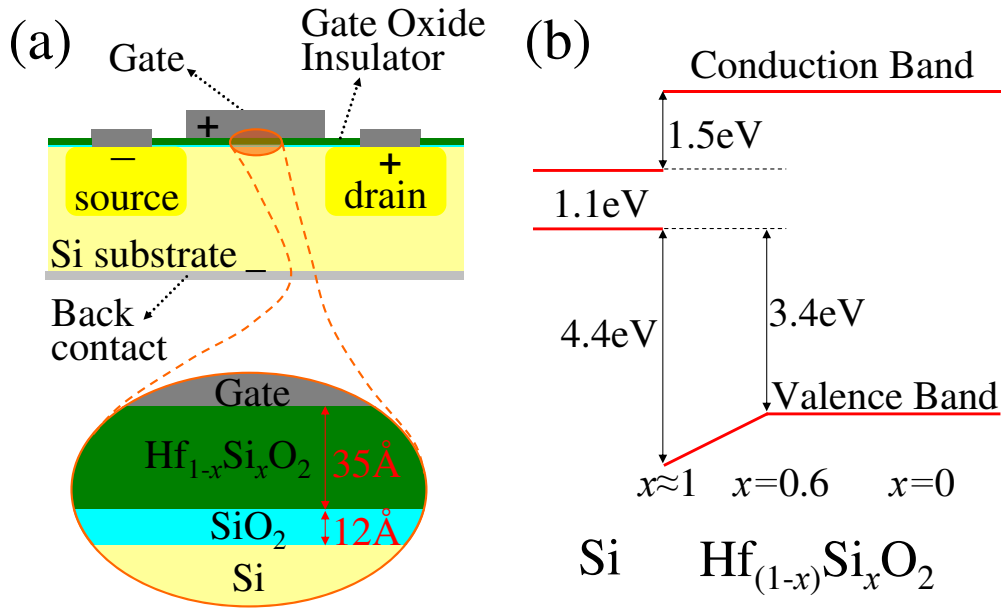


Figure 3.1: (a) Schematic diagram of complementary metal-oxide-semiconductor (CMOS) device, and of high-$\kappa$ dielectric stack structure. (b) Conduction and valence band offsets with respect to Si of Hf-silicates as a function of alloy composition.

However the problem of poor interface quality with Si remains. A partial solution is to engineer stack structures with an interlayer of $SiO_2$ or oxynitride [see Fig. 3.1(a)]. Although this approach introduces an extra interface, this new interface is between Si and $SiO_2$ and therefore of very high quality. The interface between the interlayer and the high-$\kappa$ material is also much better than the original because $SiO_2$ is amorphous. In order to guarantee device performance, the interfaces between ultrathin material layers must be carefully characterized. Cur-

rent linear optical techniques such as ellipsometry are of little use since they can't distinguish between bulk and interface signals. In this chapter SHG will be used to study $Hf_{(1-x)}Si_xO_2$ $(0 \leq x \leq 1)$ samples. It will be shown to be sensitive to growth conditions, and a viable explanation of the observed trends will be offered.

## 3.1 Samples and experimental setup

Hf-based dielectric films are amorphous in their as-deposited state [118, 119]. However, the films phase separate into $HfO_2$-rich and $SiO_2$-rich domains when subjected to rapid thermal anneals [119–121]. This separation can enhance electric field non-uniformities, roughness, and charge trapping, thus compromising device performance and reliability. But in microelectronic device fabrication anneals are routinely used, among other things for dopant diffusion. So a full characterization of the effects of annealing is essential to understanding, managing, and controlling their impact on device fabrication. The Hf-silicates phase separation has been characterized by post-anneal structural diagnostics including transmission electron microscopy, x-ray absorption [119, 122] and scattering [121, 122], photoemission spectroscopy [123], vacuum ultraviolet spectroscopy [122], medium energy ion scattering [124], and AFM [125, 126]. However an *in-situ* diagnostic technique, such as SHG, is highly desirable in order to be able to monitor the growth of the films in real time, and correct any problems that might arise without having to wait for post-anneal characterization. In this work several stack structures consisting of Hf-silicates on Si with a $SiO_2$ interlayer were grown in order to perform a systematic second-harmonic study.

Two sample sets were grown at SEMATECH's facilities. First, a set of

$Hf_{(1-x)}Si_xO_2$ samples (from now on referred to as "set 1") with different Si contents. The preparation started with a HF-last treatment of the Si(001) substrate (p-type, $\rho = 15\,\Omega$cm) for cleaning. Next, ozonated water (HCl 0.2%) was used to grow a stoichiometric $SiO_2$ interlayer with a target thickness of 12 Å. The last step was to use atomic layer deposition to grow amorphous $Hf_{(1-x)}Si_xO_2$ films with a target thickness of 35 Å, the films had silicate contents of $x$=0 (i.e. pure $HfO_2$), 0.3, 0.45, and 0.65. For each $x$ two wafers were processed. One wafer of each $x$ was left as deposited, and the other identical wafer was annealed at 700°C for 60 s in a 30 Torr ammonia atmosphere. Table 3.1 shows the characteristics of each sample from this set including the actual interlayer and silicate thicknesses as measured by ellipsometry.

| Sample number | Si content ($x$) | Annealed | Interlayer thickness (Å) | Hf-silicate thickness (Å) |
|---|---|---|---|---|
| 1 | 0 | no | 16 | 35 |
| 2 | 0 | yes | 16 | 33 |
| 3 | 0.3 | no | 17 | 36 |
| 4 | 0.3 | yes | 17 | 33 |
| 5 | 0.45 | no | 18 | 39 |
| 6 | 0.45 | yes | 18 | 32 |
| 7 | 0.65 | no | 10 | 27 |
| 8 | 0.65 | yes | 5 | 28 |

Table 3.1: Sample set 1, with varying Si content ($x$). In all cases the substrate is p-type Si(001) with resistivity of 15 Ωcm, and the interlayer is $SiO_2$. For each $x$, the sample can be left as deposited (no anneal) or be annealed at 700°C for 60 s in a 30 Torr ammonia atmosphere.

A second sample set (from now on referred to as "set 2") was grown to characterize changes in the SHG signal due to annealing conditions. The samples were grown using the same substrate and preparation procedure as for set 1. All samples

in set 2 have a Si content of $x$=0.45, *i.e.* their structure is $Si/SiO_2/Hf_{0.55}Si_{0.45}O_2$, their interlayer is ≈12 Å thick and the silicate film is ≈35 Å. One wafer was left as-deposited and all the others were annealed in the same ambient conditions as for the other set but with temperatures going from 600°C to 1000°C in 100°C increments for either 10 or 60 s. A summary of this sample set is presented in Table 3.2. A high quality $Si/SiO_2$ sample ($x$=1) was also grown on an identical substrate to be used as control.

| Sample number | Annealing temperature (°C) | Annealing time (s) |
|---|---|---|
| 1 | 600 | 10 |
| 2 | 600 | 60 |
| 3 | 700 | 10 |
| 4 | 700 | 60 |
| 5 | 800 | 10 |
| 6 | 800 | 60 |
| 7 | 900 | 10 |
| 8 | 900 | 60 |
| 9 | 1000 | 10 |
| 10 | 1000 | 60 |

Table 3.2: Sample set 2 with varying annealing conditions. In all cases the substrate is p-type Si(001) with resistivity of 15 Ωcm, and the interlayer is $SiO_2$ (≈12 Å). All samples were annealed at the shown temperature and time in a 30 Torr ammonia atmosphere.

The experimental setup used to generate SH signals is shown on Fig. 3.2. The laser source was an unamplified Ti:Sapphire oscillator with pulse duration $\tau_p \approx 30$ fs, central wavelength $\lambda = 745$ nm, 76 MHz repetition rate, and 165 mW average power just before the sample. The beam passed through a thin film polarizer at Brewster's angle to ensure a p-polarized beam. The polarization could be changed with an achromatic half-waveplate. After going through 1 mm of red

colored glass filter, the pulses were focused onto the sample at f/30, at 45° incident angle using a spherical mirror in near-axis geometry to avoid aberrations. The sample holder, consisting of a computer controlled rotational stage, was mounted on a translational stage for focusing adjustments. After recollimation, spectral filtering (using blue colored glass to eliminate fundamental and higher harmonics), and polarization selection, the reflected SHG was detected with a photomultiplier tube (PMT) connected to a photon counter. A split-off portion of the beam from the first surface of the polarizer was used to produce a reference SHG signal in transmission from $Z$-cut quartz to normalize against laser drifts.

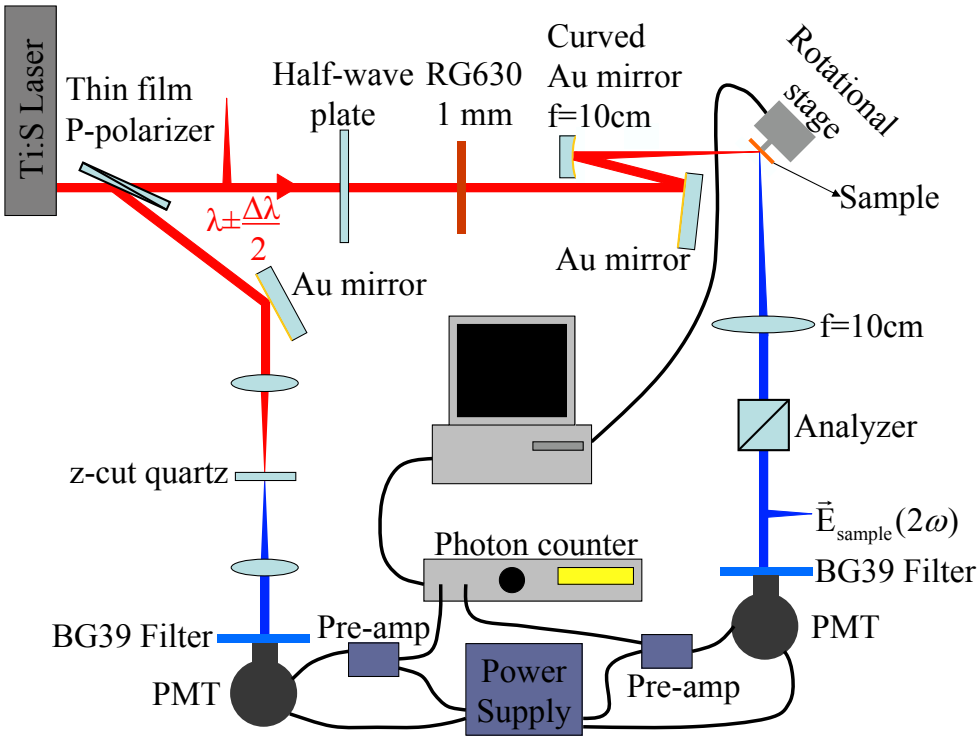


Figure 3.2: Experimental setup used for RA-SHG. Z-cut quartz plate is used for normalization against laser fluctuations. The laser pulse was ≈30 fs long centered at 745 nm.

## 3.2 Results

The behavior of the SHG signal under different input/output polarizations was studied first. Figure 3.3 shows the Rotational Anisotropic SHG (RA-SHG) pattern for different polarization combinations from two samples with $x = 0.3$, but different annealing histories (one as-deposited, the other annealed at 700°C for 60 s). All the other samples in set 1 gave similar results and therefore are not shown. The vertical scale has been renormalized (to facilitate comparison between polarizations) and thus should not be directly compared with other figures.

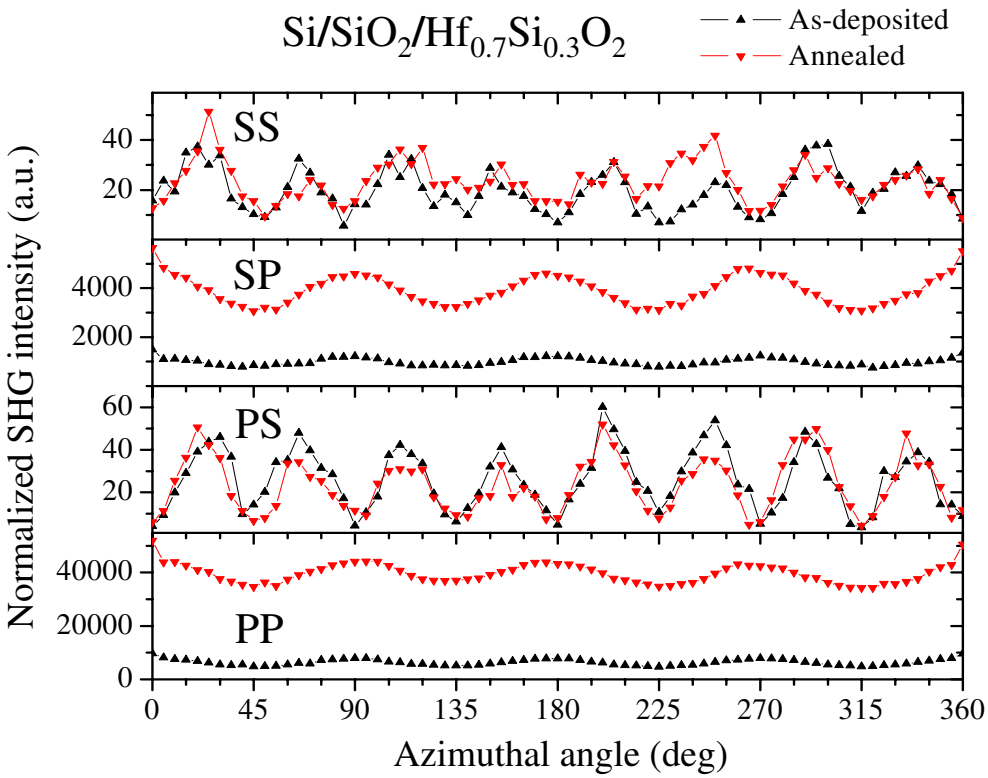


Figure 3.3: RA-SHG from $Si/SiO_2/Hf_{0.7}Si_{0.3}O_2$ with different polarization combinations. From top to bottom: S-in/S-out, S-in/P-out, P-in/S-out, and P-in/P-out. Scale has been re-normalized to reflect relative signal strengths. Black (red) triangles represent as-deposited (annealed) samples.

As it is clear from this figure, the P-polarized SHG intensity ($I^{(2\omega)}_{P-out}$) shows a 4-fold anisotropic oscillation riding on an isotropic background that can be modeled by the Fourier sum

$$I^{(2\omega)}_{P-out} = |a_0^{P-out} + a_4^{P-out} \cos 4\phi|^2, \tag{3.2}$$

where $\phi$ is the angle between the incident plane and the [110] direction. Meanwhile, the S-polarized patterns consist of an 8-fold anisotropic oscillation with no isotropic background which can be represented as $I^{(2\omega)}_{S-out} = |a_4^{s-out} \cos 4\phi|^2$. The S-polarized SHG signal level was roughly 100 times weaker than the P-polarized case. The coefficients in Eq. (3.2), and their analogs for S-polarized SHG, can be written out explicitly using Eqs. (1.8)-(1.15) and the expression for the intensity in terms of the SH field. $a_0$ originates primarily from the dipolar nonlinear susceptibility $\chi^{(2),S}_{ijk}$ of the interfaces, and $a_4$ from the quadrupolar susceptibility $\chi^{(2),Q}_{ijkl}$ of the Si bulk.

Figure 3.4 contains RA-SHG intensity measurements taken with P-in/P-out polarization from samples with varying silicate contents (set 1). The left panel corresponds to SHG from as-deposited samples, and the right panel to annealed ones. As noted above, $I^{(2\omega)}_{pp}$ displayed 4-fold sinusoidal oscillations on a isotropic background (note that the angular range on the plots has been restricted for clarity).

The SH intensity exhibits two strong $x$- and annealing-dependent trends: (1) Among as-deposited samples (Fig. 3.4, left panel), $I^{(2\omega)}_{pp}$ from $Si/SiO_2/HfO_2$ ($x$=0) was anomalously strong, almost 8 times stronger than from the control $Si/SiO_2$ sample, and 3 to 5 times stronger than from the ternary alloy dielectric ($x$=0.3, 0.45 and 0.65) samples. (2) Annealing at 700°C for 60 s (Fig. 3.4,

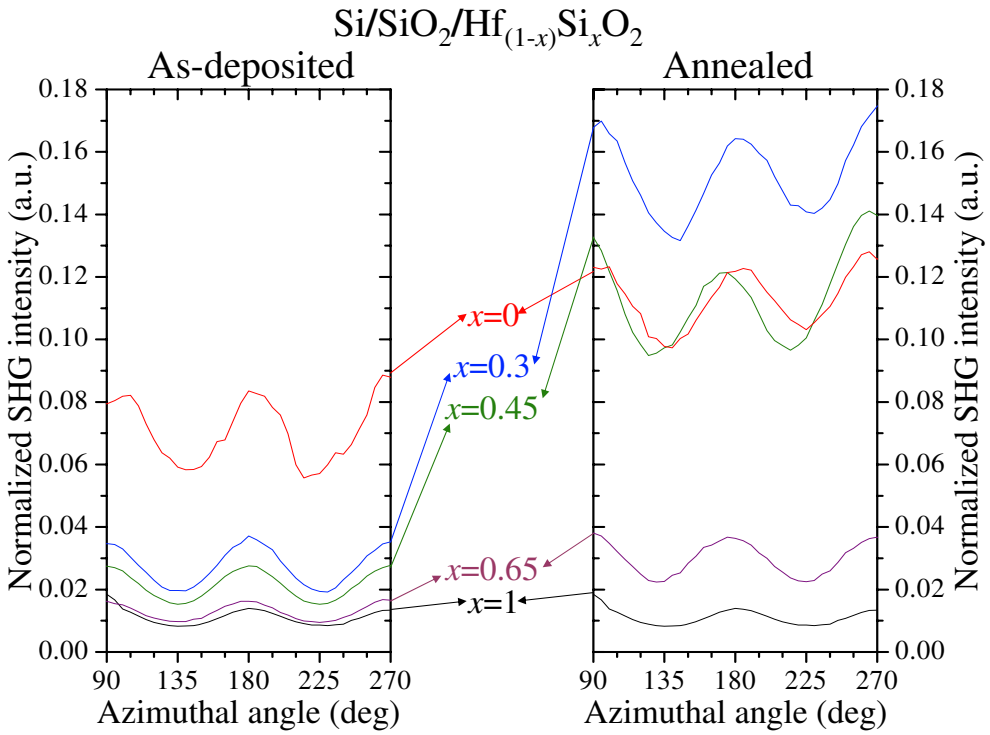


Figure 3.4: RA-SHG (P-in/P-out) from $Si/SiO_2/Hf_{(1-x)}Si_xO_2$ for the silicate contents shown. Left (right) panel represents as-deposited (annealed for 60 s at 700℃) samples. For brevity, only the azimuthal angle range $90° < \phi < 270°$ is shown.

right panel) selectively enhanced SHG from the silicate samples by factors of 3 to 5. SHG from $x$=0.3, 0.45 samples became comparable in strength to SHG from $Si/SiO_2/HfO_2$ ($x$=0). By contrast, annealing enhanced SHG from $Si/SiO_2/HfO_2$ by only $\sim$ 20%. Similar trends were observed using other polarization combinations. All RA-SHG data fit very well to Eq. (3.2) with the $x$- and annealing-dependence assigned entirely to the isotropic, dipolar SHG coefficient $a_0^{pp}$.

Figure 3.5 illustrates how $I_{pp}^{(2\omega)}$ from $Hf_{0.55}Si_{0.45}O_2$ depends on annealing temperature ($T$ = 600°C to 1000°C in 100°C increments), and duration ($\tau$=10 s on left panel, and 60 s on right panel). SHG intensity for both annealing times,

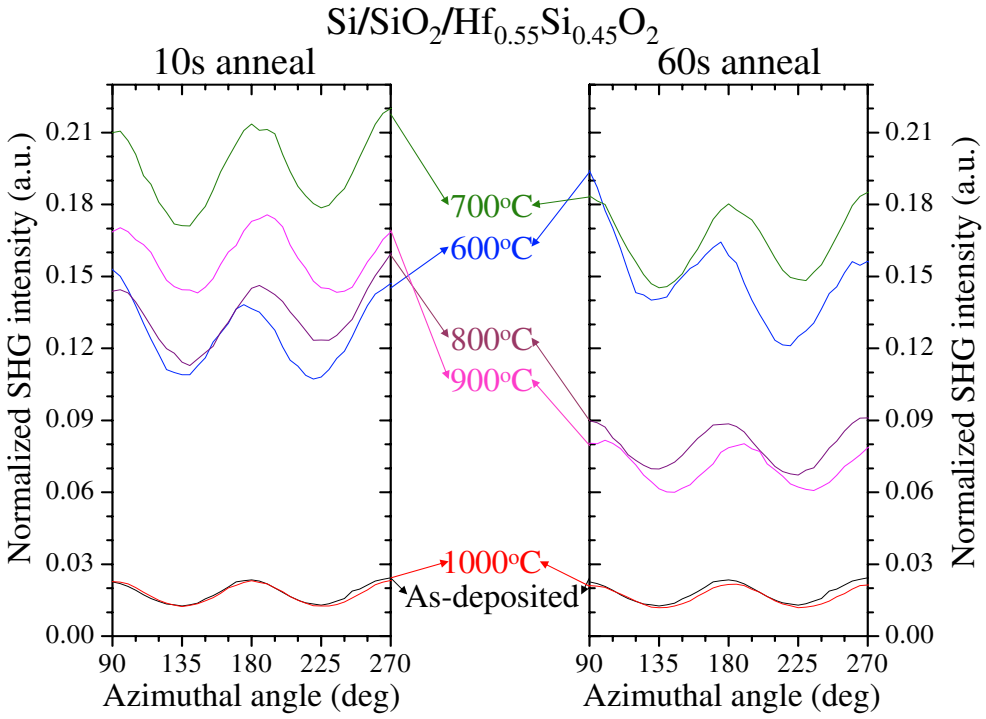


Figure 3.5: RA-SHG (P-in/P-out) from $Si/SiO_2/Hf_{0.55}Si_{0.45}O_2$ for the annealing temperatures shown. Left (right) panel is for 10 s (60 s) anneal. For brevity, only the azimuthal range 90° to 270° is shown.

increases with $T$ until it peaks at $T \approx 700$°C and then starts to decrease reaching the level for as-deposited samples at $T \approx 1000$°C. The rise and fall of the signal with $T$ is faster for the samples subjected to longer anneals. This is expected since whatever the mechanism that changes the SHG signal is, for longer anneals it has more time to act. A model for this mechanism will be presented in the next section. Another interesting trend is that for both annealing times the signal level for $T = 700$°C is very similar.

In order to better understand these trends, a curve fit to Eq. (3.2) was done with $a_0^{pp}$ and $a_4^{pp}$ as free parameters. The results of the fit vs. annealing temperature are shown in Fig. 3.6. The left (right) panel of this figure contains

coefficient $a_0^{pp}(T)$ $[a_4^{pp}(T)]$ for $\tau = 10\,\mathrm{s}$ (black circles) and $60\,\mathrm{s}$ (red squares). The error bars in both panels are only from the fitting procedure and do not include an estimate of other experimental errors. Within error, $a_4^{pp}$ is almost constant (varies approximately by 10%) and roughly 15 times smaller than $a_0^{pp}$. This means that the dipolar interface contribution was responsible for the signal variations while the bulk contribution didn't change with annealing.

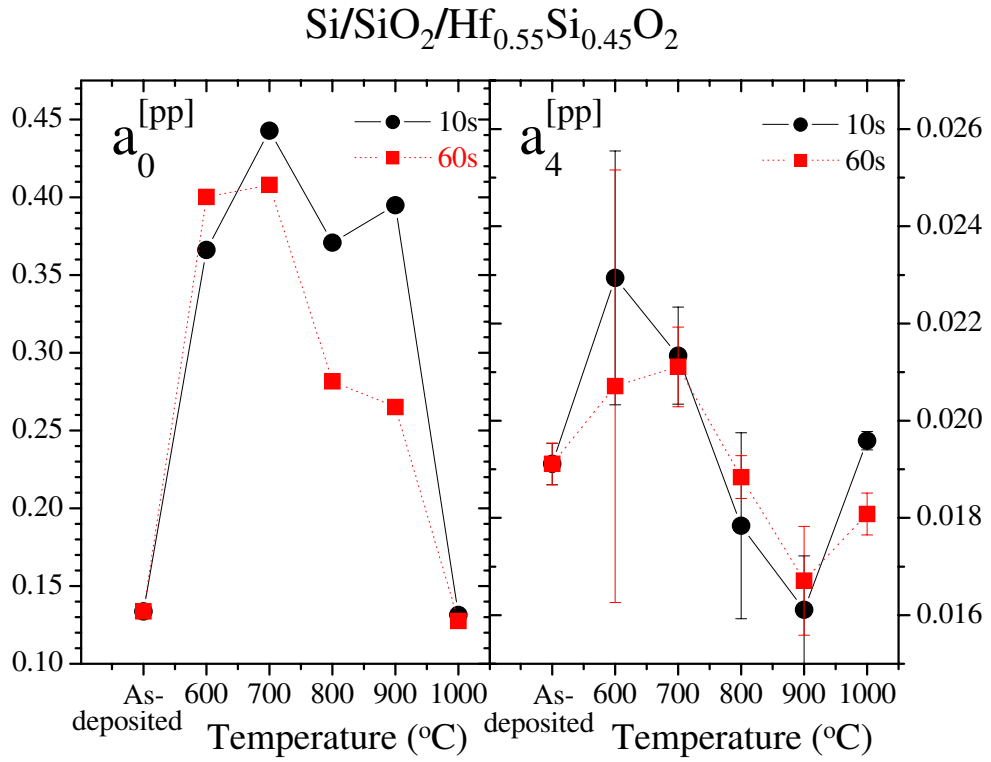


Figure 3.6: Fourier coefficients $a_0$, and $a_4$ extracted from curve fits of Eq. (3.2) to RA-SHG (P-in/P-out) data from Fig. 3.5. Note that first point is for as-deposited samples.

SHG spectroscopy can provide further information about the interface by looking at changes of spectral lineshape and peak positions with composition and annealing conditions. SHG spectra were acquired from samples in set 1, the

procedure was to measure RA-SHG of each sample at different wavelengths then the Fourier coefficients were obtained using the same fitting procedure described above. The laser was operated in a narrow-bandwidth ($\tau_p \sim 100$ fs) $\lambda$-tunable configuration that allows a fundamental wavelength range from 710 nm to 850 nm. The corresponding SH photon energies are $2.8 < h\nu_{SH} < 3.45$ eV, enough to look at the Si $E_1$ resonance [91].

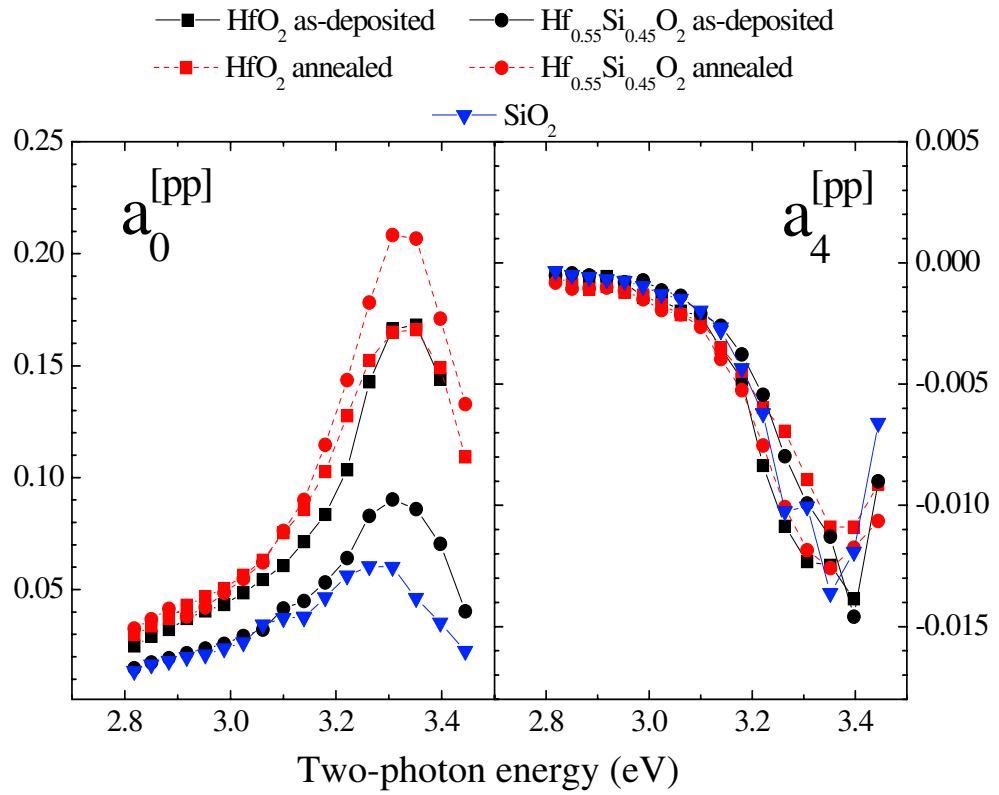


Figure 3.7: Examples of SHG spectra from as-deposited and annealed $Si(001)/SiO_2/HfO_2$, $Si(001)/SiO_2/Hf_{0.55}Si_{0.45}O_2$, and $Si(001)/SiO_2$ structures. All data is in P-in/P-out polarization. The annealed was done at 700°C for 60 s.

Figure 3.7 presents the extracted Fourier coefficient spectra ($a_0^{pp}(h\nu_{SH})$ and $a_4^{pp}(h\nu_{SH})$) from samples of different $x$ and annealing treatments. The results shown are for as-deposited (black) and annealed (red) samples of $HfO_2$ (squares),

$Hf_{0.55}Si_{0.45}O_2$ (circles), and $SiO_2$ (triangles). The scale in this figure should not be compared directly with the other figures since the laser system was operating with different pulse duration and average power. The spectra for $a_4^{pp}(h\nu_{SH})$ (right panel) is, much smaller than $a_0^{pp}(h\nu_{SH})$, independent of $x$ and annealing, and peaked at the $E_1$ energy $h\nu_{SH} = 3.4\,\text{eV}$ of bulk Si. For $a_0^{pp}(h\nu_{SH})$ the $E_1$ SH resonance retains the same position ($h\nu_{SH} = 3.3$ eV) and shape regardless of $x$ or annealing, the only changes were on the overall SHG amplitude. The resonances of the high-$\kappa$ structures are slightly blue-shifted with respect to $Si/SiO_2$. These spectra suggest that $a_0^{pp}(h\nu_{SH})$ is a sum of a $\nu$-dependent, but $x$- and $T$-independent, contribution $a_0^{Si/SiO_2}(h\nu_{SH})$ coming from the $Si/SiO_2$ interface and an $x$- and $T$-dependent, but spectrally non-resonant (NR), contribution $a_0^{NR}$ originating from elsewhere in the sample.

## 3.3 Explanation of observed trends

In this section a possible explanation for the trends observed in the experimental data is presented. Fomenko and co-workers claim that SHG trends similar to those observed in this work are caused by charge trapped at oxygen vacancy defects in the high-$\kappa$ films [127]. This trapped charge could modify the sample nonlinear optical response through electric-field-induced second-harmonic (EFISH) generation. In this effect, the presence of an electric field breaks the centrosymmetry of the bulk and introduces a new source for second harmonic production [85]. However, two features of our results suggest that EFISH, at most, plays only a minor role in the sample behavior. First, a SH signal coming from EFISH in bulk Si would peak at the bulk $E_1$ energy $h\nu_{SH} = 3.4\,\text{eV}$. If the trapped charge interpretation were correct, the interfacial part of the SHG

structures spectra should be pulled from 3.3 eV towards 3.4 eV [93], which is not observed (see Fig. 3.7, left panel). Second, the oxygen vacancy defect densities of the samples, which are believed to constitute the trap centers, were characterized by spectroscopic ellipsometry (SE) measurement of sub-$HfO_2$ band gap (4 to 6 eV) absorption [116]. The absorption strength turned out to be uncorrelated with annealing or composition, contrary to what the trapped charge hypothesis would imply.

The model offered to explain the observed trends is based on the idea that $a_0^{NR}$ (as defined at the end of previous section) originates primarily from Si-O-Hf bond units in the dielectric film [69]. These bond units are strongly polarizable as reflected by the fact that they create a high linear $\kappa$. But because they lack centrosymmetry, they also acquire second-order dipole moments $\vec{p}_i^{2\omega}$ when irradiated by a strong pump beam at $\omega$. Their resonant frequency can be approximated by the Hf-silicate band gap ($\sim 6$ eV), which is far above $h\nu_{SH}$, therefore they contribution to the SH response is far from resonance for the spectral range considered here, in agreement with observations. Figure 3.8 depicts qualitatively how Si-O-Hf bond units, represented as green arrows from Si to Hf, can produce the observed SHG trends. In this figure, part (a) represents the as-deposited case and part (b) the situation after annealing; the schematic $I^{(2\omega)}$ vs. $\phi$ panels are a reminder of relative signal strength.

First, an analysis of the as-deposited trends is presented. For $Si/SiO_2$ [Fig. 3.8(a), left], there are no Si-O-Hf bonds and consequently the observed signal is weak consisting solely of $a_0^{Si/SiO_2}$ contributions. For $Si/SiO_2/HfO_2$ ($x$=0), Si-O-Hf bonds are present only at the $SiO_2/HfO_2$ interface, and are mutually aligned

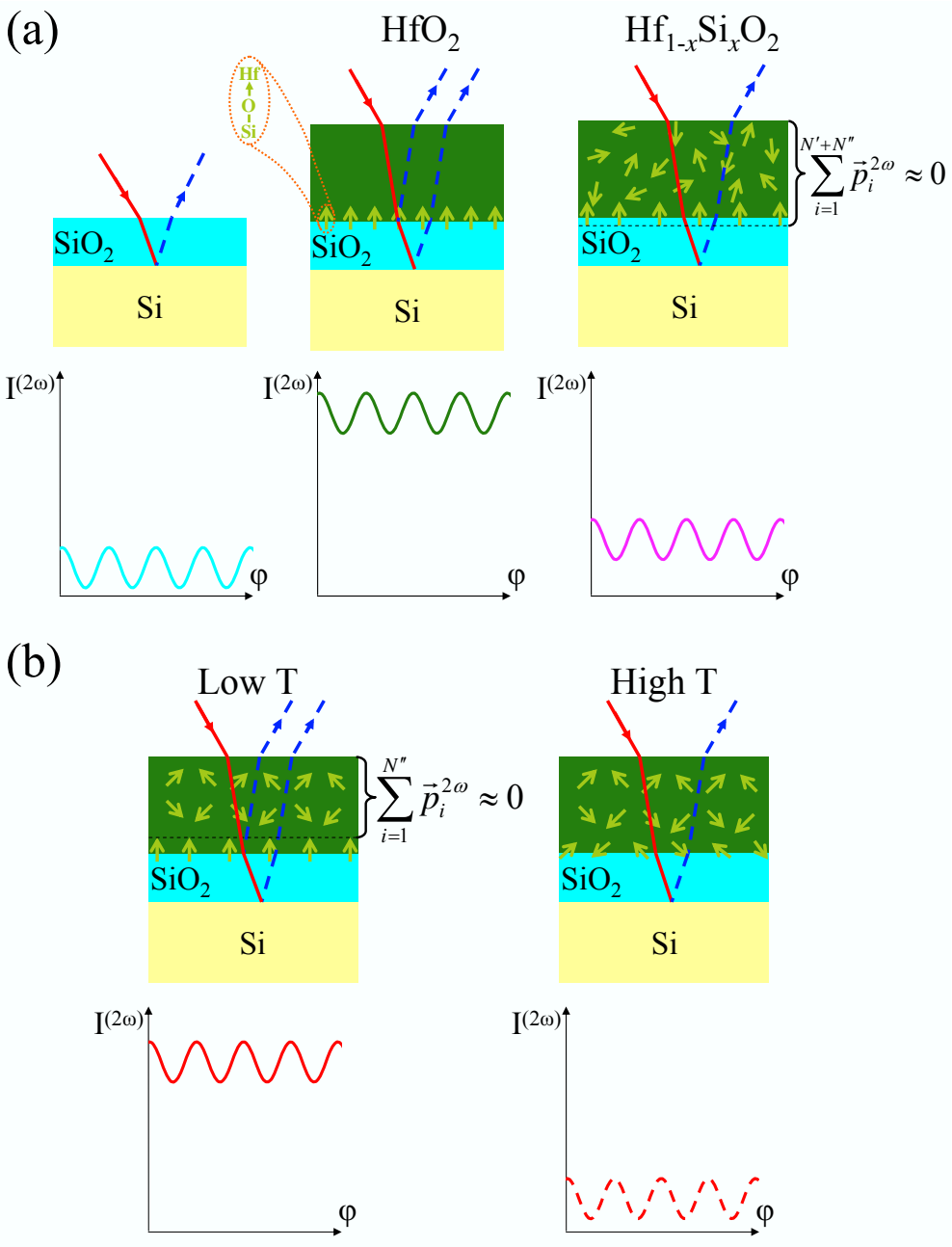


Figure 3.8: Heuristic model of SHG by Si-O-Hf bond units (green arrows) in (a) as-deposited (left: Si/$SiO_2$; middle: Si/$SiO_2$/$HfO_2$; right: Si/$SiO_2$/Hf-silicate) and (b) annealed (left: $\sim$ 700℃; right: $\sim$ 1000℃) structures. Red solid line: 745 nm input beam; blue dashed lines: SH output beam(s). The I vs. $\phi$ curves are to illustrate relative signal levels coming from each structure.

toward the $HfO_2$ film [Fig. 3.8(a), middle]. Assume that there are $N$ of them per unit area. This leads to a large interfacial SH polarization $\sum_{i=1}^{N} \vec{p}_i^{2\omega} \approx N\vec{p}_i^{2\omega}$, and thus a large $a_0^{NR}$ that augments $a_0^{Si/SiO_2}(h\nu_{SH})$, and qualitatively explains the stronger p-polarized SHG from this sample (Fig. 3.4, left). For the as-deposited $x$=0.3, 0.45 and 0.65 samples [Fig. 3.8(a), right], a reduced number $N' < N$ of aligned Si-O-Hf bonds is again present at the $SiO_2$/Hf-silicate interface. In addition, $N''$ Hf-O-Si bonds with net opposite orientation protrude from the interface into the bulk of the amorphous Hf-silicate film. Evidently the latter, on average, cancel most of the SH polarization of the interfacial bonds — *i.e.* $\sum_{i=1}^{N'+N''} \vec{p}_i^{2\omega} \approx 0$ — leaving a net SHG response resembling that of $Si/SiO_2$ (Fig. 3.4, left).

Meanwhile, for the annealed samples the trends can be explained as follows. After annealing $HfO_2$ crystallites can form in the bulk of the film [119, 125], but are randomly oriented and therefore make no net contribution to SHG. Thus, the density and orientation of interfacial Si-O-Hf bonds, and total SHG remain approximately unchanged. For a low temperature anneal the network of $N''$ Hf-O-Si bond units within the bulk of the dielectric film re-arranges [Fig. 3.8(b), left], because Hf-silicates are unstable against separation into $SiO_2$ and $HfO_2$ domains. Details of the phase separation depend on composition: for $x$=0.3, 0.45 spinodal decomposition dominates, and domains remain amorphous; for $x$=0.65, $HfO_2$ crystallites nucleate and grow [120, 121]. In both cases, however, the planar layer of $N'$ Si-O-Hf bonds is a preformed, thermally stable domain boundary. It is proposed that this layer and its SH polarization $\sum_{i=1}^{N'} \vec{p}_i^{2\omega} \approx N'\vec{p}_i^{2\omega}$ remain intact upon annealing to 700°C, while the network of $N''$ Hf-O-Si bond units within the Hf-silicate bulk re-arrange in mutually canceling orientations such that $\sum_{i=1}^{N''} \vec{p}_i^{2\omega} \approx 0$. Post-anneal SH polarization, $N'\vec{p}_i^{2\omega}$, is thus comparable to that of

$Si/SiO_2/HfO_2$, qualitatively explaining the selective enhancement of $I_{pp}^{(2\omega)}$ in Hf-silicate samples annealed at 700°C (Fig. 3.4, right). With TEM, separated $SiO_2$ and $HfO_2$ domains become evident only after $\sim 900$°C anneals. The strong effect of 600-700°C anneals on SHG indicates its remarkable, unique sensitivity to the incipient stages of phase separation.

Finally, the decreasing SHG intensity (*i.e.* $a_0^{NR}$) observed following $T > 800$°C anneals (Fig. 3.5) must be attributed to thermal disordering of the aligned layer of $N'$ interfacial Si-O-Hf dipoles [Fig. 3.8(b), right]. Interfacial Hf need only diffuse an atomic layer for the interfacial SH polarization $\sum_{i=1}^{N'} \vec{p}_i^{2\omega}$ to drop from $\sim N'\vec{p}_i^{2\omega}$ to $\sim 0$. Indeed medium energy ion scattering shows that Hf diffusion into the oxide interlayer becomes significant at $T \sim 900$°C [124]. It must be noted that although the measurements presented this far were done *ex-situ*, there's nothing that could prevent the use of SHG directly on the sample growth chamber. This potential capability is unique to second harmonic since, as already discussed, all other characterization techniques require UHV environments, modifications of the sample or turn out not to be sensitive enough for ultrathin films.

## 3.4 Conclusions

In this chapter high-quality $Si(001)/SiO_2$/Hf-silicate structures with varying Si content and annealing conditions have been characterized by RA- and spectroscopic SHG. The results demonstrate that SHG can probe phase separation in high-$\kappa$ dielectric films non-invasively. SHG from Hf-silicate stacks is strongly affected by rapid anneals under conditions that induce phase separation. In marked contrast, SHG from control $HfO_2$ and $SiO_2$ stacks shows little effect under iden-

tical anneals. Thus SHG appears to be sensitive to annealing-induced structural modification in the Hf-silicate films. The strong dependence of SHG on dielectric composition and annealing was attributed qualitatively to the changing alignment of hyperpolarizable Si-O-Hf bonds. This model explains all the observed experimental trends and is consistent with the microscopic observations done using other techniques. Although our present results were obtained *ex situ*, they show that SHG could be used for *in situ*, real-time monitoring of phase separation kinetics during annealing.

# Chapter 4

# SHG phase measurements

So far, this work has been completely devoted to SHG intensity measurements neglecting the phase information. However, close to resonance the complex nature of the nonlinear susceptibility becomes important and for a full characterization both amplitude and phase must be measured. As was pointed out in the first chapter several different sources contribute to the SH production. The total signal will be the coherent sum of all the contributions, therefore phase differences between these SHG sources can result in dramatic changes in the observed SHG amplitude.

As already mentioned in chapter 1, an experimental technique to measure the relative phase between fundamental and SH light was introduced shortly after Franken's first SHG experiments [17]. In this method a reference SHG signal was produced from a KDP (potassium-dihydrogen-phosphate) crystal located inside the same chamber that contained the sample. The optical path length between the reference signal and the sample SHG was varied in a controlled way by admitting dry air at different pressures. The pressure in the chamber modified the dispersion of air which in turn changed the time delay between reference and sample pulses. The detected signal was the superposition of both SHG fields and produced an interferogram when recorded as a function of pressure. From this information the relative SHG phase was extracted. Second harmonic phase is typically measured

using variations of this scheme, for example: instead of varying the pressure, the distance between reference and sample is varied to change the optical path length. Independently of the specific implementation this method is very time consuming because a scan of some sort must be done to vary the optical path length between the pulses. Another disadvantage is that the retrieved phase information is for a single wavelength, to obtain spectroscopical phase data the laser must be tuned which also requires long time and is prone to misalignments [128]. This situation is in sharp contrast with linear surface/interface optical probes like spectroscopic ellipsometry, for which real-time acquisition of spectral amplitude and phase is routine.

As discussed in chapter 2, the broad bandwidth ($h\Delta\nu \sim 0.2\,\mathrm{eV}$) of ultrafast laser sources enables spectroscopic SHG intensity data acquisition by spectral dispersion of the generated SH light, instead of laser tuning [93, 129]. Frequency domain interferometric second harmonic (FDISH) is a phase measurement technique, introduced by Wilson and coworkers in 1999 [130], that takes advantage of the broad $h\Delta\nu$ of ultrafast sources. FDISH enables rapid, accurate SH phase measurements without any moving parts, and without any scans during the experiment. These features are reflected in enormous time savings during phase data acquisition. In previous work this technique has been used to characterize the phase changes due to an applied dc electric field in a MOS capacitor [130], and to extract phase information with micron size resolution using FDISH microscopy [131, 132].

In this chapter, the versatility of FDISH is illustrated and exploited through a series of bulk and surface SHG phase measurements showing variations with az-

imuthal angle and time (with resolution better than one second), and extraction of the relative phase amongst the three tensor components of the nonlinear susceptibility $\chi^{(2)}$ of a Si(001)-dielectric interface. Before presenting the results a brief introduction to FDISH will be given, explaining the experimental setup, the phase retrieval algorithm, and the normalization procedure used to remove spectral artifacts coming from the reference.

## 4.1 Introduction to FDISH

A short introduction to the FDISH technique, used for all phase measurements in this chapter, will be presented. First a description of the experimental setup will be given. After this, the algorithm employed for retrieving spectral phase from the measured interferograms will be presented.

### 4.1.1 Experimental setup

Figure 4.1 shows the experimental FDISH set-up [130]. It is very similar to the arrangement described for RA-SHG measurements except in three aspects: laser source, insertion of the reference film before the sample, and detection system. The Ti:Sapp laser oscillator was operated in the broad bandwidth configuration ($\Delta\lambda$ ranging from 40 to 80 nm). After the curved mirror used to focus the fundamental onto the sample, a reference nonlinear film deposited on a $\sim$1 mm thick glass slide was inserted with the film facing the input beam side. The film consisted of a tricyanovinylaniline (TCV) poled polymer [133] spin casted on glass, its refractive index and extinction coefficients, taken from this reference, are shown in the inset of Fig. 4.1. The SHG generated from the reference propagated collinearly with the fundamental, but was temporally delayed by $\tau \approx 1$ ps due to

group velocity dispersion in the glass substrate. At the sample, the fundamental pulse generated another SH pulse in reflection, while the reference pulse was simply reflected. Both SH pulses were sent sequentially into a spectrometer where they interfered generating an interferogram that was recorded by a liquid nitrogen cooled charge coupled device (LN CCD). As mentioned before, the absence of any moving parts means a stable optical alignment over long periods. The total acquisition time depends only on CCD readout time, and on signal strength which determines the optimal integration time for each interferogram. Spectral resolution was set by spectrometer resolving power, and CCD pixel size.

### 4.1.2 Phase retrieval

The algorithm to retrieve the SHG phase from the recorded interferograms is based on Fourier analysis of the frequency domain signal [130, 134, 135]. In essence, the procedure consist of 3 steps: (1) The interferogram is converted to the time domain using a Fourier transform resulting in three peaks at $t = -\tau, 0, \tau$. (2) The peak at $t = \tau$ is selected by a window function and moved to the origin. (3) An inverse Fourier transform is used to go back to the frequency domain and the phase is obtained as the argument of the resulting complex function.

A more detailed description of the procedure is now given introducing some details that are necessary for a computer based analysis. The first step is changing the interferogram to be a function of frequency instead of wavelength. Also, in order to use fast Fourier transforms (denoted by $\mathfrak{F}$), the frequency range must be divided in $2^n$ equally spaced frequency increments. This can be accomplished by using a spline. Then a window function that goes to zero for points outside the interferogram must be applied to reduce numerical noise in the wings of the

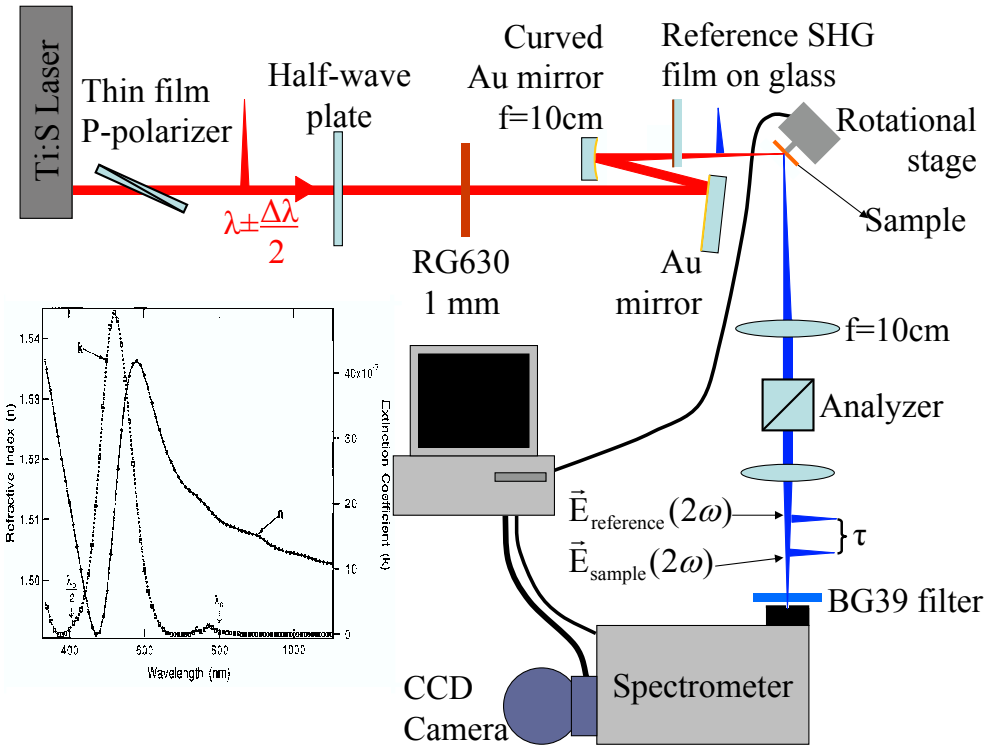


Figure 4.1: FDISH setup. A thin film polarizer and half-wave plate control polarization of the input pulses (typically 15 to 30 fs). A concave mirror focuses the pulses onto the sample with 45° incidence angle through a thin SH reference film: tricyanovinylaniline (TCV) poled polymer deposited on glass. The analyzer selects the desired output SH polarization. The inset shows the refractive index and the extinction coefficient of the TCV film taken from Ref. [133].

signal. The mathematical form of the interferogram in the frequency domain is:

$$I(\Omega) = \left| E_{sample}(\Omega) + E_{ref}(\Omega) e^{-\imath \Omega \tau} \right|^2, \tag{4.1}$$

$E_{sample}$, $E_{ref}$ are SH fields of sample and reference respectively. The expressions in terms of the spectral amplitude and phase of these fields ($\mathcal{E}_{sample}(\Omega) e^{\imath \phi_{sample}(\Omega)}$,

and $\mathcal{E}_{ref}(\Omega)e^{\imath\phi_{ref}(\Omega)})$ can be substituted in the last equation to obtain:

$$I(\Omega) = \overbrace{|\mathcal{E}_{sample}(\Omega)|^2 + |\mathcal{E}_{ref}(\Omega)|^2}^{a(\Omega)} + \underbrace{\mathcal{E}_{sample}(\Omega)\mathcal{E}^*_{ref}(\Omega)e^{\imath\Delta\phi(\Omega)}e^{\imath\Omega\tau}}_{b^*(\Omega)} + \underbrace{\mathcal{E}^*_{sample}(\Omega)\mathcal{E}_{ref}(\Omega)e^{-\imath\Delta\phi(\Omega)}e^{-\imath\Omega\tau}}_{b(\Omega)}, \quad (4.2)$$

where $^*$ denotes the complex conjugate and $\Delta\phi(\Omega) = \phi_{sample} - \phi_{ref}$. At this point the first $\mathfrak{F}$ to the time domain is performed resulting in $A(t) + B^*(t+\tau) + B(t-\tau)$ with $A(t) = \mathcal{F}[a(\Omega)]$ and $B(t) = \mathcal{F}[b(\Omega)]$. $A(t)$ is centered at $t = 0$, $B^*(t+\tau)$ at $t = -\tau$, and $B(t-\tau)$ at $t = \tau$, explaining the three peaks that were mentioned before. Next the peak at $t = \tau$ is selected using a square window and translated to the origin in time. Finally $\mathfrak{F}^{-1}$ is applied to this function to recover $b(\Omega)$, and $\Delta\phi(\Omega)$ is obtained as the argument of this complex function.

Since the reference film can have spectral features that could obscure the interpretation of $\Delta\phi(\Omega)$, another measurement is made substituting the sample by a piece of $Z$-cut quartz. Quartz is spectrally flat in the fundamental and SHG regions. Subtracting these two results, the phase difference between sample and quartz standard is obtained eliminating any possible spectral artifacts.

## 4.2 Results and discussion

In this section the SHG phase of four different material systems will be studied using FDISH. In the first example, meant to illustrate the ease of data acquisition, the SHG phase of bulk GaAs was measured as a function of the azimuthal position of the crystal. Although the predicted phase variation is simple, it has not been measured previously. Second, FDISH is used to study crystalline

quartz where azimuthal variations of SH phase create a sign ambiguity. In order to allow quartz to be used as a standard in FDISH measurements, the ambiguity needs to be resolved, this is accomplished using information from intensity RA-SHG. The next application is the measurement of the absolute SHG phase from each of the three independent tensor components $\chi_{xxz}$, $\chi_{zxx}$, and $\chi_{zzz}$ of the Si(001)/high-$\kappa$ dielectric interface. Finally an illustration of the ability of FDISH to acquire data in real-time will be given by measuring the time dependent phase changes from $Si/SiO_2$ and $Si/SiO_2/HfO_2$ with a resolution better than one second.

### 4.2.1 RA-SHG phase shift from GaAs

Although GaAs has a cubic crystal lattice similar to Si, it is noncentrosymmetric due to the presence of two different atomic species (zincblende structure). Its point group is $\overline{4}$2m, and it has a very strong second order *bulk* nonlinear susceptibility with only one nonzero tensor component $\chi^{(2),GaAs}_{xyz}$. This subsection will consider the SHG phase variation of reflected SHG from a native oxidized GaAs(001) (4mm symmetry) as a function of the angle of azimuthal rotation. Even though there is a small *isotropic* contribution coming from the (001) surface, it will be neglected since it is approximately 16 times smaller than the bulk signal. For the P-in/P-out polarization combination, the azimuthal ($\phi$) dependence of the SH field has the following mathematical form [136, 137]:

$$I^{(2\omega)}_{pp} = \left|E^{(\omega),GaAs}_{p}\right|^2 \left|a^{(2)}_{pp}\chi^{(2),GaAs}_{xyz}\cos 2\phi\right|^2, \tag{4.3}$$

where the coefficient $a^{(2)}_{pp}$ includes Fresnel and geometrical factors, $E^{(\omega),GaAs}$ is the fundamental field inside the material, $\chi^{(2),GaAs}$ is given in crystallographic coordinates, and $\phi = 0°$ corresponds to the plane of incidence along [110]. The

upper left panel of Fig. 4.2 sketches the behavior of $E_{pp}^{(2\omega),GaAs}$ based on Eq. (4.3), and shows the sign variations of $\cos 2\phi$ over a 360° rotation. These sign changes, located at $\phi = 45°$, 135°, 225° and 315°, should be manifested as a phase shift of $\pi$ rad in $E_{pp}^{(2\omega),GaAs}(\phi)$.

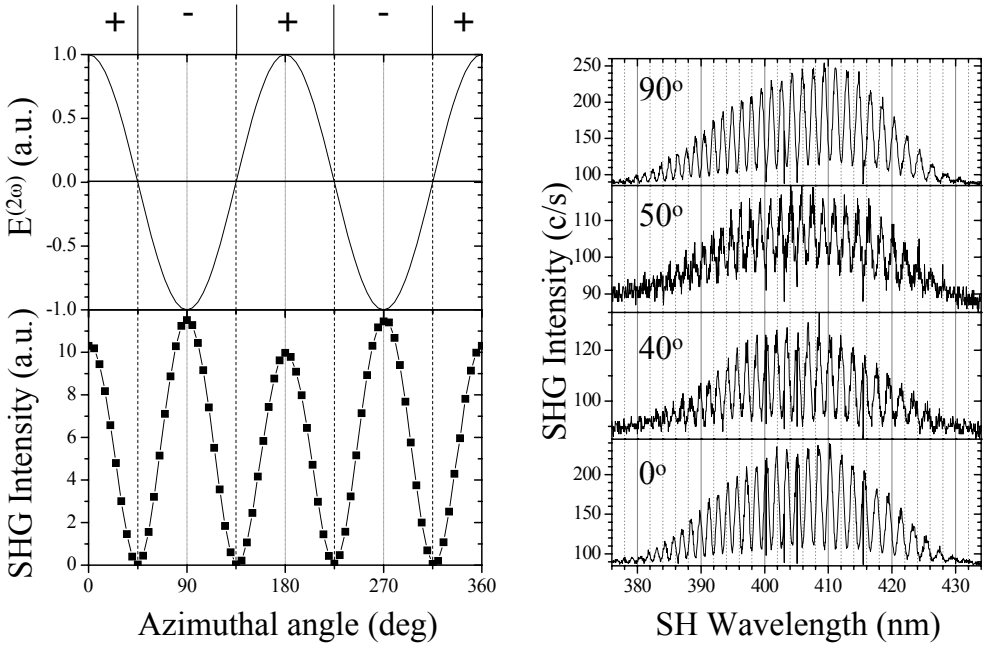


Figure 4.2: Rotationally anisotropic SHG and FDISH from GaAs. Left panel: expected sign variation of the second harmonic field (top) and azimuthal variation of the SHG intensity (bottom). The different peak heights result from interference with the much weaker surface contribution. Right panel: FDISH interferograms at different azimuthal orientations showing phase shift ($\Delta\phi \approx \pi$ rad) between 40° and 50°. All data were taken with P-in/P-out polarization.

FDISH was used to acquire interferograms as the azimuthal angle of the GaAs sample was varied in 5° steps. The right panel of Fig. 4.2 shows four interferograms, as recorded by the CCD camera, taken at $\phi$ = 0, 40, 50, and 90°. The data for $\phi = 45°$ is not shown because the signal is down to noise level since $E_{pp}^{(2\omega),GaAs}(\phi = 45°) = 0$. A $\pi$ rad phase shift is indeed clearly observed

between $\phi = 40°$ and $50°$. Similar shifts are observed at the other 3 expected angles corroborating the prediction.

These phase shifts are also represented indirectly in the RA-SHG intensity signal shown in the lower left panel of Fig. 4.2. They are manifested through the presence of peaks with different heights. The "major" ("minor") peaks come from the constructive (destructive) interference between the weak isotropic surface signal and the positive (negative) anisotropic bulk contribution.

### 4.2.2 SH phase measurement of $Z$-cut quartz

Quartz belongs to the 32 symmetry class (hexagonal). As mentioned above, in its $Z$-cut form (cutting plane perpendicular to crystallographic $Z$-axis), it is used to eliminate any spectral artifacts coming from the nonlinear film used as reference in FDISH. The advantage of quartz over other material is that its two independent nonzero bulk susceptibility components, $\chi^{(2),Qz}_{xxx} = -\chi^{(2),Qz}_{xyy} = -\chi^{(2),Qz}_{yxy} = -\chi^{(2),Qz}_{yyx}$ and $\chi^{(2),Qz}_{xyz} = \chi^{(2),Qz}_{xzy} = -\chi^{(2),Qz}_{yzx} = -\chi^{(2),Qz}_{yxz}$, are real and positive at the fundamental and second harmonic wavelengths of Ti:Sapp lasers. Of these susceptibility components, $\chi^{(2),Qz}_{xyz}$ is much smaller (almost two orders of magnitude) than $\chi^{(2),Qz}_{xxx}$ and its contribution is isotropic [138]. Any contributions from the surface will be neglected.

The resulting SHG field is composed of an isotropic term coming from the weak $\chi^{(2),Qz}_{xyz}$ component, and a 3-fold anisotropic term related to $\chi^{(2),Qz}_{xxx}$. For the Q-in/S-out polarization combination, with Q-polarization being a linear polarization at 45° between the S and P polarizations, the expression for the SH

field is:

$$E_{QS}^{(2\omega),Qz} = \left\{ a_{QS}^{(0),Qz} \chi_{xyz}^{(2),Qz} + a_{QS}^{(3),Qz} \chi_{xxx}^{(2),Qz} \cos 3\phi \right\} \left| E_{Q}^{(\omega),Qz} \right|^2, \qquad (4.4)$$

where coefficients $a_{QS}^{(0),Qz}$, and $a_{QS}^{(3),Qz}$ depend on Fresnel factors and geometry but do not contain any hidden contributions from the susceptibility, and $E_{Q}^{(\omega),Qz}$ is the fundamental field inside the quartz. The strong anisotropic term will dominate the signal, but it will flip its sign every 60°, when $\cos 3\phi$ goes from positive to negative and viceversa. This sign variation will introduce a $\pi$ rad phase ambiguity compromising the usefulness of quartz as a phase standard. This phase shift is clearly shown in Fig. 4.3 by the two FDISH interferograms taken at $\phi = 0$, and 60° in Q-in/S-out polarization.

This ambiguity can be resolved by noting that the positive and real isotropic $\chi_{xyz}^{(2),Qz}$ contribution, although very weak, is also present in the total signal. Thus a situation similar to that of the previous subsection arises, and it is expected that a combination of major and minor peaks will be observed in the RA-SHG intensity. This is indeed the case as can be seen in the inset of Fig. 4.3 (note that the angular range has been restricted for clarity); there are major peaks at $\phi = 0, 120$, and 240° and minor peaks at $\phi = 60, 180$ and 300°. Since the major peaks correspond to the orientations for which the two susceptibility components are in phase, *i.e.* the anisotropic contribution is positive, these peaks identify the azimuthal positions at which the quartz has to be located when used as standard for phase measurements. Similar analyses apply for other polarization combinations.

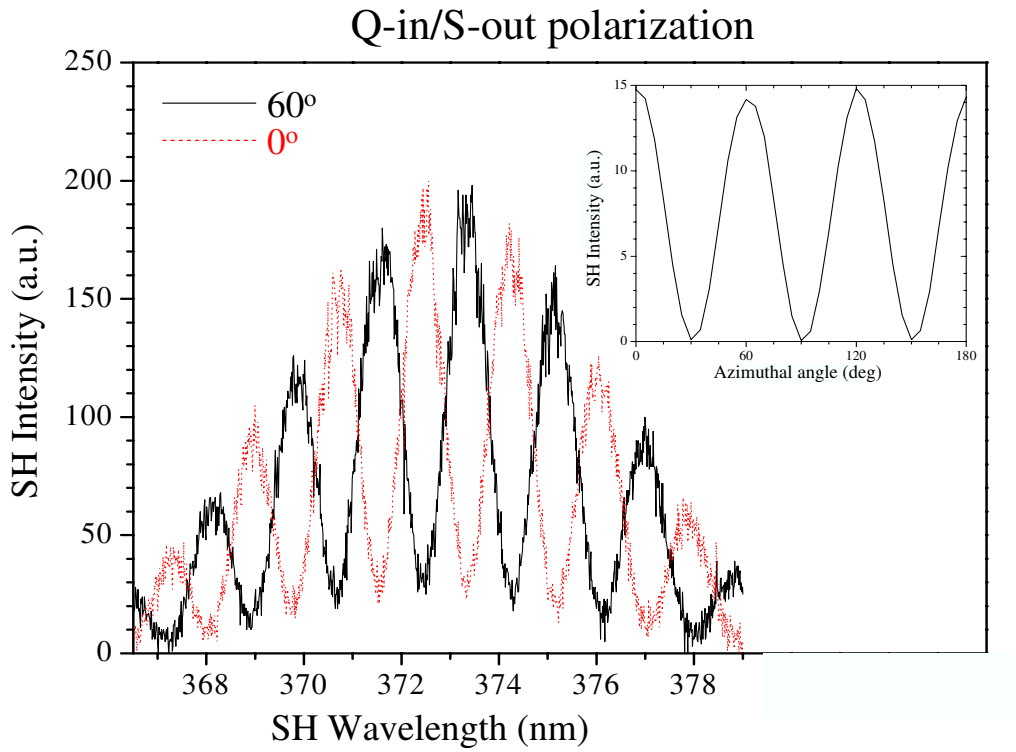


Figure 4.3: Quartz FDISH interferograms taken at azimuthal angles $\phi$=60° (black solid line) and $\phi$=0° (red dotted line). Inset: RA-SHG showing a peak height variation every 60°. Both measurements are in Q-in/S-out polarization.

### 4.2.3 Phase of Si(001) nonlinear susceptibility

The importance of Si(001)-dielectric interfaces has already been discussed. In this section the phase of the three independent components of the Si susceptibility will be measured using FDISH. To do this, FDISH will be used in strategic polarization configurations and sample orientations chosen to isolate each component to a good approximation [139, 140]. The phases relative to the fundamental phase are straightforwardly determined after normalization against $Z$-cut quartz. The bulk quadrupole contribution will be neglected for the current analysis because of its weakness. To justify this assumption note that the S-in/S-out SHG

signal originates solely from the bulk quadrupolar component [see Eq. (1.9) with $\Psi = 90°$]; but SHG intensity in this configuration is much weaker than in P-out configuration (see Fig. 3.3).

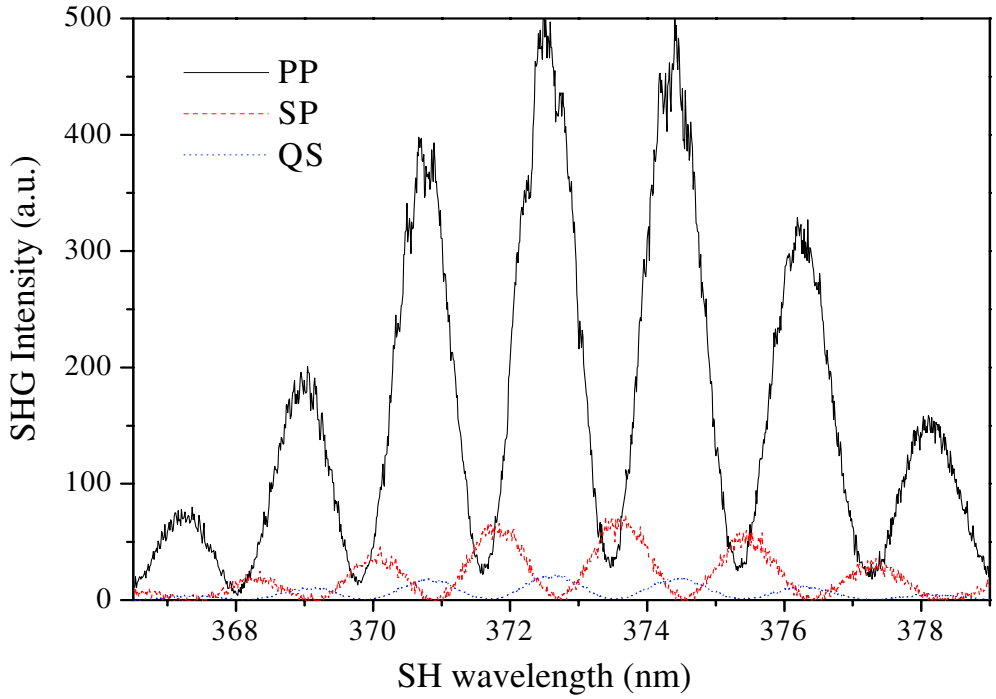


Figure 4.4: FDISH interferograms from a Si(001)-dielectric structure for P-in/P-out, S-in/P-out and Q-in/S-out polarization combinations. The sample [100] axis is oriented along the incident plane.

All measurements were done with the sample [100] axis in the plane of incidence. The results are shown in Fig. 4.4 for three polarization combinations chosen to isolate the different susceptibility components: P-in/P-out, S-in/P-out, and Q-in/S-out. S-in/P-out polarized SHG depends only on $\chi^{(2),S}_{zxx}$, while Q-in/S-out only on $\chi^{(2),S}_{xxz}$ as can be seen from the expressions given in chapter 1. Although the P-in/P-out configuration originates from a linear combination of all 3 interface tensor components, based on its much stronger amplitude relative to the other two

polarizations it is concluded that $\chi^{(2),S}_{zzz}$ dominates the signal.

An analysis of the interferograms (without including the quartz normalization) for P-in/P-out and S-in/P-out, following the procedure described above, gives a relative phase shift between $\chi^{(2),S}_{zzz}$ and $\chi^{(2),S}_{zxx}$ of approximately $0.75\pi$ rad. A similar analysis for P-in/P-out and Q-in/S-out, to obtain the relative phase between $\chi^{(2),S}_{zzz}$ and $\chi^{(2),S}_{xxz}$, gives $0.09\pi$ rad. In extracting the absolute phases the phase shifts due to linear and nonlinear complex Fresnel factors need to be taken into account. Using tabulated values for the complex index of refraction of Si [94], these phase shifts can be calculated. The result is that the total phase shift from the Fresnel factors is, for all cases, at most $0.1\pi$ rad. Absolute phases with respect to the driving field are then determined by using the quartz standard instead of the sample, as described before. The final result is that the phases of $\chi^{(2),S}_{zzz}$, $\chi^{(2),S}_{xxz}$, and $\chi^{(2),S}_{zxx}$ are $0.4\pi$ rad, $0.5\pi$ rad, and $0.79\pi$ rad respectively. All the measurements have an uncertainty of around $0.1\pi$ rad coming mainly from signal and numerical noise.

### 4.2.4 Time dependent SH phase measurements

Time-dependent (TD) variation of SH *intensity* from ultrathin oxides in Si(001) has been observed and well known since the mid 90's [61, 141]. This time variation takes place in a time scale of seconds to minutes and typically consists of an increase of the SHG signal with time during laser exposure followed by a gradual return to the original signal level after the laser is blocked for several minutes.

The physical mechanism responsible for TD-SHG is schematically pre-

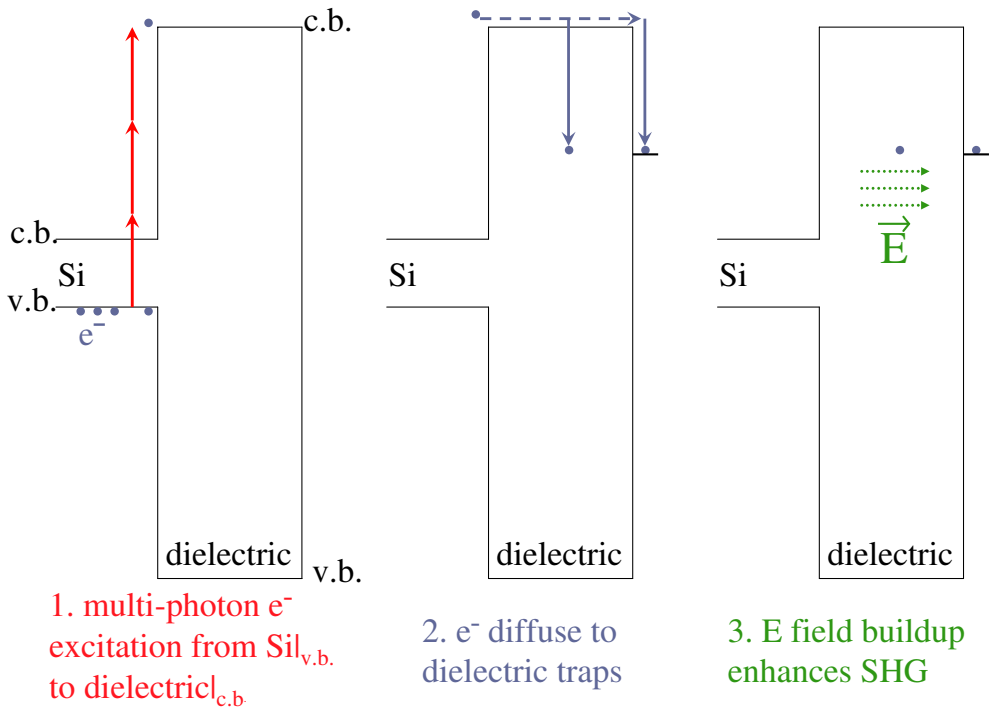


Figure 4.5: Schematic explanation of TD-SHG: (1) Electrons are excited from Si valence band (v.b.) to dielectric conduction band (c.b.) by the fundamental laser field. (2) Once in dielectric c.b., electrons drift, in a time scale of seconds to minutes, and get trapped inside the bulk or in surface traps. (3) Trapped carriers induce a dc electric field in the dielectric that changes with time. This dc field contributes to the total SHG signal through EFISH.

sented in Fig. 4.5. As shown in panel (1) of this figure, the fundamental beam induces multiphoton excitation of electrons from the Si valence band to the oxide conduction band. The number of photons required obviously depends on the wavelength of the fundamental light and on the band offsets between dielectric and Si. It is also possible for holes to be excited from Si conduction band to dielectric valence band, but for many Si/dielectric systems the band offset between these bands is larger than for electrons. Since a higher number of photons are required for the excitation of holes to take place this process has a lower probability than

for electrons, and usually can be neglected. After the excitation, the electrons can drift across the oxide and be trapped either in the bulk of the oxide or in its surface, this process takes place in seconds to minutes and sets the time scale for TD-SHG. The resulting electric field buildup gradually enhances the SHG signal through electric-field-induced SH (EFISH) generation [142].

The source of the EFISH signal is the breaking of the centrosymmetry of the material due to the presence of a dc electric field ($\boldsymbol{E}^{dc}$). The nonlinear polarization corresponding to this effect can be written in the following way [143]:

$$\boldsymbol{P}^{(2\omega),\,EFISH} = \overset{\leftrightarrow}{\chi}^{(3),\,Si} : \boldsymbol{E}^{(\omega),\,Si}\boldsymbol{E}^{(\omega),\,Si}\boldsymbol{E}^{dc}. \tag{4.5}$$

It is important to note that the nonlinear susceptibility in this equation is the third order dipolar bulk Si susceptibility. This, in principle, should make the EFISH contribution much larger than the surface dipole SHG, however the contribution of this term is limited by the escape depth of the SHG radiation from the bulk of Si, and/or by the screening length of the dc field (whichever is smaller).

A proper model of EFISH must take into account retardation of the radiation due to dispersion, penetration depth of the fundamental, escape length of the SHG, multiple reflection interference effects in the oxide layer, and the dc field spacial distribution inside Si. Assuming that the dc field is varying only in the $z$-direction, the final expression for the SH field from EFISH that encompasses all these elements is given by [144]:

$$\boldsymbol{E}^{(2\omega),\,EFISH} = F^{(2\omega)}\left[F^{(\omega)}\right]^2 \chi_{eff}^{(3),\,Si} I^{(\omega)} \mathbf{p} e^{\imath \mathbf{k}^{(2\omega)}\cdot\mathbf{R}} \int_0^\infty E^{dc}(z') e^{\imath\left(\mathbf{k}^{(2\omega)}+2\mathbf{k}^{(\omega)}\right)\cdot\hat{\mathbf{k}}z'} \mathrm{d}z'. \tag{4.6}$$

In this equation $F^{(2\omega)}$ and $F^{(\omega)}$ represent nonlinear and linear Fresnel factors, $\chi_{eff}^{(3),\,Si}$ is a linear combination of $\overset{\leftrightarrow}{\chi}^{(3),\,Si}$ elements which depends on the geometry,

$I^{(\omega)}$ is the fundamental intensity, $\mathbf{R}$ is the point at which SHG is measured, and $\mathbf{k}^{(2\omega)}$, $\mathbf{k}^{(\omega)}$ are wavevectors of SHG and fundamental radiation.

The EFISH field will display time variation (in a time scale of seconds to minutes) due to the temporal dependence of the dc electric field inside Si. The SH radiation from EFISH will add up coherently with the fields generated by bulk quadrupole and surface dipole terms. Even when the EFISH term keeps a constant phase in time, the total SHG field can have a time dependence as schematically represented in the phasor diagram of Fig. 4.6. In this figure the amplitude of the EFISH field changes with time but it has a constant phase while the interfacial SHG field is assumed to be constant, as it is clear from the diagram the resulting total SHG signal will have a time variation in both phase and amplitude.

As mentioned before, many papers have reported TD-SHG intensity measurements, and some groups have used this effect in attempts to characterize the oxide electronic trap lifetime or density [62–65, 85, 127, 145–147]. However all of the existing papers deal only with the time dependency of the SHG intensity ignoring the corresponding SH *phase* time dependence. In this section the fast acquisition time of FDISH will be exploited to perform such measurements for the first time. The samples used were native-oxidized Si(001)/$SiO_2$, and as-deposited Si/$SiO_2$/$HfO_2$ (sample 1 of set 1, see Table 3.1).

In the experiments, both the amplitude and phase of the SHG signal were measured, although not simultaneously. To measure intensity time dependence the FDISH set-up was reconfigured by removing the reference film and sending the SHG signal to a photomultiplier tube connected to a photon counter, bypassing the spectrometer and CCD (see Fig. 4.1). All signals were recorded in P-in/P-

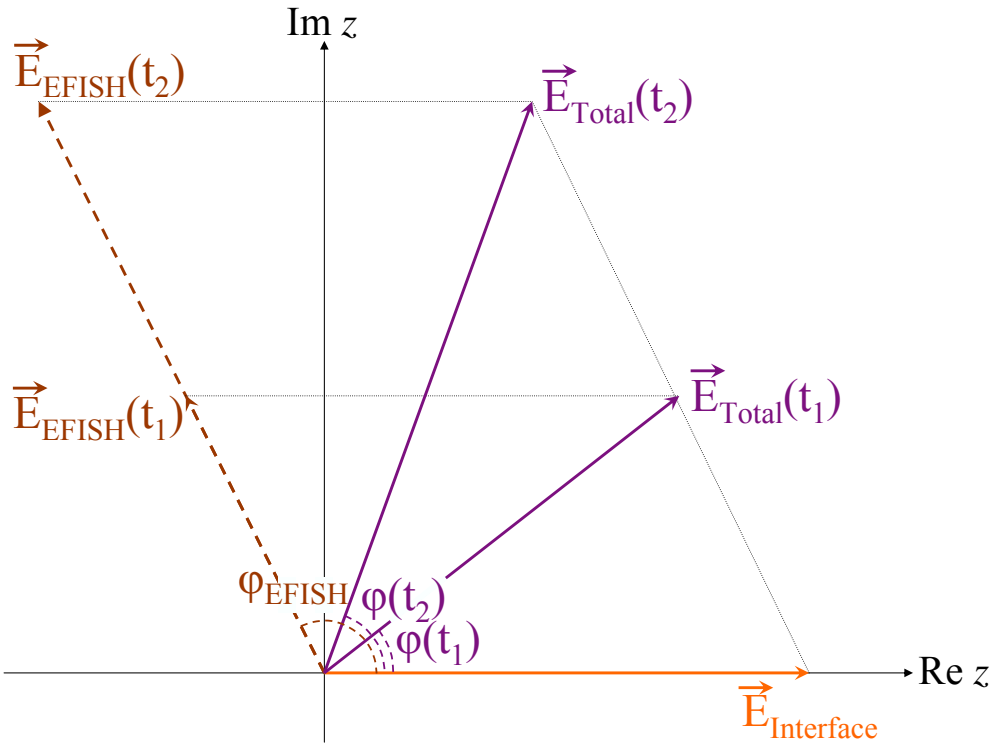


Figure 4.6: Phasor diagram explanation of TD-SHG. $\vec{E}_{\mathrm{EFISH}}(t)$ has constant phase, $\phi_{\mathrm{EFISH}}$, but its amplitude changes with time. $\vec{E}_{\mathrm{Interface}}$ and $\vec{E}_{\mathrm{EFISH}}(t)$ add coherently to give $\vec{E}_{\mathrm{Total}}(t)$, which has a time dependent phase $\phi(t)$.

out polarization. The sample was azimuthally positioned at a maximum of the RA-SHG signal, then the laser beam was obstructed and the sample moved to a fresh un-exposed spot. After this, the temporal dependence of the SHG signal was recorded continuously for almost half an hour with the photon counter set to 0.4 s acquisition time. To measure the time evolution of the SH phase, the reference film was reinserted and the LN CCD camera was set to take frames continuously with a exposure time of 0.4 s per frame. The total acquisition and read-out time per frame was ≈0.8 s.

Results are shown in Fig. 4.7. The TD-SHG intensity signals (see two top

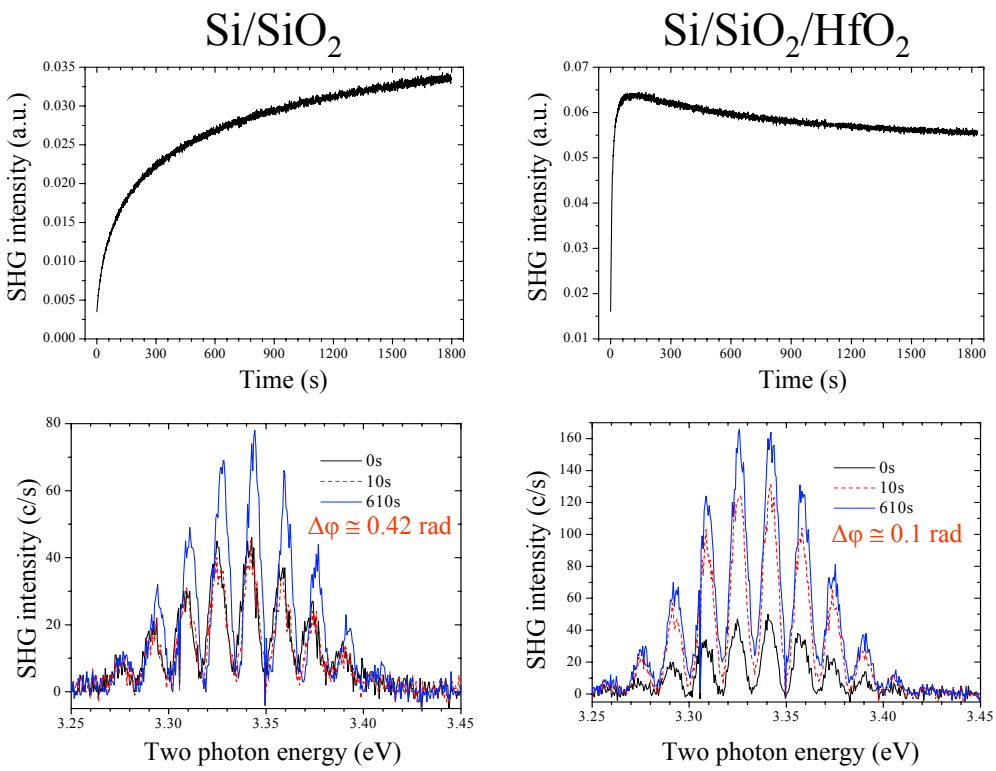


Figure 4.7: Time dependent SHG intensity (top panels) and phase (lower panels) from native-oxidized Si(001)/$SiO_2$ (left panels) and as-deposited Si(001)/$SiO_2$/$HfO_2$ (right panels). Total acquisition and read-out time for each interferogram is ≈0.8 s. All measurements done with P-in/P-out polarization.

panels) agree with measurements done by other groups [61, 68, 85]. The bottom panels show 3 of the recorded interferograms for $t$ = 0, 10, and 610 s for both systems. A phase shift of ≈0.42 rad between interferograms at 0 and 610 s is measured for the native oxide sample, while for the $HfO_2$ system the phase shift is only ≈0.1 rad. This information, together with $\chi^{(2),Si}$ from the previous subsection, could be used to deconvolve the EFISH contribution from the signal.

At least one group has suggested that oxygen is crucial, acting as a catalyzer, for carrier trapping processes in ultrathin $SiO_2$ layers [62, 148, 149]. In or-

der to probe if this is true also for ultrathin high-$\kappa$ dielectric layers, experiments in high vacuum (HV) were performed. The sample used was sample 3 from set 1 (see Table 3.1). The procedure was: (1) The sample was put in a high vacuum (HV) chamber which then was evacuated to $10^{-9}$ Torr but the temperature was not varied and remained room temperature (RT), TD-SHG was recorded using a PMT. (2) Laser was blocked, sample was moved to fresh spot and then heated to 150°, before taking data the sample was cooled back to RT, and TD-SHG was then taken. (3) Same as in previous number but temperature was 600°. (4) Laser was blocked, sample was moved to fresh spot and then exposed to ambient air, after returning to HV conditions, with no heating, TD-SHG was taken at RT.

Figure 4.8 shows that the TD-SHG signal strength clearly depends not on vacuum conditions but on temperature. The results are in contradiction to the reports in the literature mentioned above where other authors observed either a very weak time dependent effect or no effect at all under UHV conditions, in sharp contrast with results shown in black curve of Fig. 4.8. To explain the discrepancy, an explanation of the trends observed in this work will be offered first. It is proposed that the TD-SHG signal decrease with sample heating (see purple and red curves of Fig. 4.8) because the contaminants sitting on top of the sample are being desorbed. The contaminants act as catalyzers for carrier trapping. The higher the temperature, the more TD-SHG decrease. These trends are schematically illustrated on the right hand of the experimental curves. The proposed hypothesis is further validated by the signal recovery after re-exposure to ambient air with no further heating (see blue curve). If the presence of oxygen in the ambient were responsible for TD-SHG signal quenching, we should not observe such strong response in vacuum (see black and blue curves). It is possible

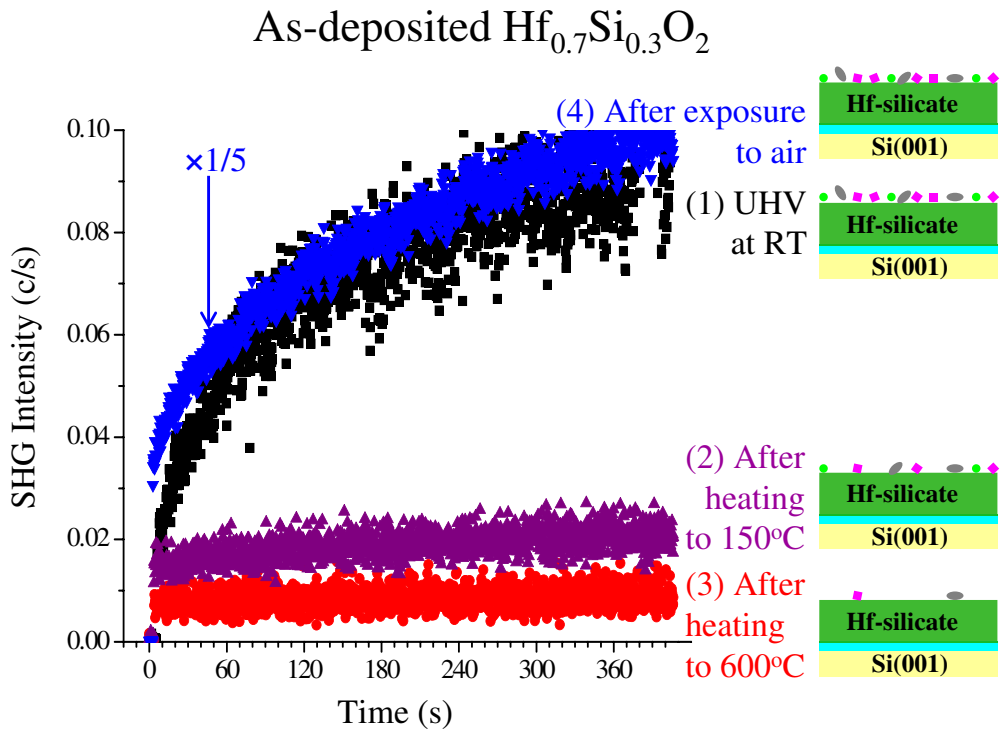


Figure 4.8: Time dependent SHG intensity variation with temperature in high vacuum (HV). (1) Chamber is evacuated to $10^{-9}$ Torr but kept at room temperature (RT). (2) Sample heated to 150° and cooled to RT before taking data. (3) Sample heated to 6000° and cooled to RT before taking data. (4) Sample exposed to ambient air and then returned to HV conditions. All measurements done with P-in/P-out polarization.

that the different interpretation given in the cited references came from the fact that their measurements were done using UHV conditions, which strongly suggest that they had to bake their chamber for long periods of time and therefore desorb the contaminants from the surface, quenching the signal. Since contaminants play a role in TD-SHG, one must be very careful when using this technique to characterize trapping lifetimes or densities.

## 4.3 Conclusions

Several examples have been used to illustrate how FDISH can provide rapid, accurate, and valuable second harmonic phase information. The examples included: azimuthal and time variations of SH phase and phase measurement of individual tensor components of $\chi^{(2)}$ from Si(001). Explanations of the observed trends were given. The examples provided here would have been extremely laborious and time consuming using conventional phase measuring techniques. In all cases, once the samples were mounted and aligned, the total acquisition time was a few minutes. Acquisition time for a single interferogram was one second or less for the samples studied here. This speed and convenience opens an unprecedented window of opportunity for real-time and spectroscopic SH phase studies.

# Chapter 5

# Conclusions and future directions

A review of the theory of second harmonic generation from Si interfaces was presented together with a compendium of relevant expressions for the non-linear surface and bulk polarizations of this system. The case of spectroscopic measurements using broad bandwidth pulses was also reviewed. Sum Frequency Generation between Ti:Sapphire pulses and white light continuum experiments were performed. It was found that handling the continuum produced by a photonic crystal fiber was extremely difficult, especially its collimation and focusing.

Rotational anisotropy (RA), spectroscopy, and time dependence SHG studies of the technologically relevant $Si/SiO_2/HfO_2$ and $Si/SiO_2$/Hf-silicate interfaces were performed. RA-SHG signal was affected by the Si content of the silicate and by the annealing history of the samples. The $Si/SiO_2$ interface dominated the spectral response of the system within the studied spectral region, but no spectral sensitivity to sample composition or annealing history were found. It was proposed that Si-O-Hf bond units are responsible for the SHG behavior, the bond units in the $SiO_2$/Hf-silicate interface are proposed to be thermally stable (at least for anneals done below 800°) while the units in the bulk of the silicate undergo phase separation during anneals. This model is consistent with observations done using other techniques such as HR-TEM. The results from the time dependent studies challenged the interpretation of a direct correlation between the charge

trap densities and the SHG time constants.

SHG phase studies of three systems were done. An expected $\pi$ phase shift during azimuthal rotations of GaAs(001) was indeed observed. The phase of the second order surface susceptibility of Si(001) was measured using polarization selection rules. For the first time, SHG phase measurements with a time resolution better than one second were done. These examples demonstrate the power and flexibility of the employed technique, frequency domain interferometric second harmonic (FDISH).

There are two main future extensions of this work. One is extending the spectral bandwidth for FDISH and the other extending the spectral bandwidth for SHG spectroscopy. The first goal could be achieved by using the WLC from only a few mm of microstructure fiber. The pulses produced by such short pieces of fiber do not present a chirp as large as that observed in this work, benefiting the FDISH signal levels. The second goal could probably be better achieved by the use of a noncollinear optical parametric amplifier (NOPA). SHG spectroscopy of the Hf samples with a much broader bandwidth could detect spectral features coming from the presence of substoichiometric oxides or, if two photon energies higher than the band gap of the Hf-silicates ($\approx 6\,\mathrm{eV}$) are used, from the Hf-silicates themselves. This information could be very valuable in monitoring the changes of the samples with different parameters.

# Bibliography


[1] A. Zangwill. *Physics at Surfaces*. Cambridge University Press, 1988.

[2] W. Mönch. *Semiconductor Surfaces and Interfaces*. Springer, second edition, 1995.

[3] J. F. McGilp, D. Weaire, and C. H. Patterson, editors. *Epioptics*. Springer, 1995.

[4] N. Bloembergen. *Nonlinear Optics*. World Scientific, fourth edition, 1996.

[5] R. W. Boyd. *Nonlinear Optics*. Academic Press, 1992.

[6] Y. R. Shen. *The Principles of Nonlinear Optics*. Wiley-Interscience, 1984.

[7] P. A. Franken, A. E. Hill, C. W. Peters, and G. Weinreich. Generation of optical harmonics. *Phys. Rev. Lett.*, 7(4):118, 1961.

[8] J. A. Armstrong, N. Bloembergen, J. Ducuing, and P. S. Pershan. Interactions between light waves in a nonlinear dielectric. *Phys. Rev.*, 127(6):1918, 1962.

[9] N. Bloembergen and P. S. Pershan. Light waves at the boundary of nonlinear media. *Phys. Rev.*, 128(2):606, 1962.

[10] B. Lax, J. G. Mavroides, and D. F. Edwards. Nonlinear interband and plasma effects in solids. *Phys. Rev. Lett.*, 8(4):166, 1962.

[11] D. F. Edwards, J. G. Mavroides, and B. Lax. *Bull. Am. Phys. Soc*, 7(1):14, 1962.

[12] R. W. Terhune, P. D. Marker, and C. M. Savage. Optical harmonic generation in calcite. *Phys. Rev. Lett.*, 8(10):404, 1962.

[13] J. Ducuing and N. Bloembergen. Observation of reflected light harmonics at the boundary of piezoelectric crystals. *Phys. Rev. Lett.*, 10(11):474, 1963.

[14] F. Brown, R. E. Parks, and A. M. Sleeper. Nonlinear optical reflection from a metallic boundary. *Phys. Rev. Lett.*, 14(25):1029, 1965.

[15] F. Brown and R. E. Parks. Magnetic-dipole contribution to optical harmonics in silver. *Phys. Rev. Lett.*, 16(12):507, 1966.

[16] J. E. Bjorkholm and A. E. Sigman. Accurate CW measurements of optical second-harmonic generation in ammonium dihydrogen phosphate and calcite. *Phys. Rev.*, 154(3):851, 1967.

[17] R. K. Chang, J. Ducuing, and N. Bloembergen. Relative phase measurement between fundamental and second-harmonic light. *Phys. Rev. Lett.*, 15(1):6, 1965.

[18] S. S. Jha. Theory of optical harmonic generation at a metal surface. *Phys. Rev.*, 140(6A):A2020, 1965.

[19] S. S. Jha. Nonlinear optical reflection from a metal surface. *Phys. Rev. Lett.*, 15(9):412, 1965.

[20] N. Bloembergen and Y. R. Shen. Optical nonlinearites of a plasma. *Phys. Rev.*, 141(1):298, 1966.

[21] N. Bloembergen, R. K. Chang, and C. H. Lee. Second-harmonic generation of light in reflection from media with inversion symmetry. *Phys. Rev. Lett.*, 16(22):986, 1966.

[22] S. S. Jha and C. S. Werke. Interband contributions to optical harmonic generation at a metal surface. *Phys. Rev.*, 153(3):751, 1967.

[23] N. Bloembergen, R. K. Chang, S. S. Jha, and C. H. Lee. Optical second-harmonic generation in reflection from media with inversion symmetry. *Phys. Rev.*, 174(3):813, 1968.

[24] C. C. Wang. Second-harmonic generation of light at the boundary of an isotropic medium. *Phys. Rev.*, 178(3):1457, 1969.

[25] F. Brown and M. Matsuoka. Effect of adsorbed surface layers on second-harmonic light from silver. *Phys. Rev.*, 185(3):985, 1969.

[26] H. J. Simon, D. E. Mitchell, and J. G. Watson. Optical second-harmonic generation with surface plasmons in silver films. *Phys. Rev. Lett.*, 33(26):1531, 1974.

[27] J. Rudnick and E. A. Stern. Second-harmonic radiation from metal surfaces. *Phys. Rev. B*, 4(12):4274, 1971.

[28] J. R. Bower. Effects of electron band structure on optical second-harmonic generation at metal surfaces. *Phys. Rev. B*, 14(6):2427, 1976.

[29] G. L. Richmond, J. M. Robinson, and V. L. Shannon. Second harmonic generation studies of intefacial structure and dynamics. *Prog. Surf. Sci.*, 28(1):1, 1988.

[30] N. Bloembergen. Surface nonlinear optics: A historical overview. *Appl. Phys. B*, 68:289, 1999.

[31] C. K. Chen, A. R. B. de Castro, and Y. R. Shen. Surface-enhanced second-harmonic generation. *Phys. Rev. Lett.*, 46(2):145, 1981.

[32] P. Guyot-Sionnest, W. Chen, and Y. R. Shen. General considerations on optical second-harmonic generation from surfaces and interfaces. *Phys. Rev. B*, 33(12):8254, 1986.

[33] J. E. Sipe, D. J. Moss, and H. M. van Driel. Phenomenological theory of optical second- and third-harmonic generation form cubic centrosymmetric crystals. *Phys. Rev. B*, 35(3):1129, 1987.

[34] J. E. Sipe, V. Mizrahi, and G. I Stegeman. Fundamental difficulty in the use of second-harmonic generation as a strictly surface probe. *Phys. Rev. B*, 35(17):9091, 1987.

[35] H. W. K. Tom, C. M. Mate, X. D. Zhu, J. E. Crowell, T. F. Heinz, G. A. Somorjai, and Y. R. Shen. Surface studies by optical second-harmonic generation: The adsorption of $O_2$, CO, and sodium on the Rh(111) surface. *Phys. Rev. Lett.*, 52(5):348, 1984.

[36] J. F. McGilp and Y. Yeh. Probing the buried metal-semiconductor interface by optical second harmonic generation: Au on Si(111) and Si(100). *Solid*

*State Comm.*, 59(2):91, 1986.

[37] D. E. Spence, P. N. Kean, and W. Sibbett. 60 fs pulse generation from a self-mode-locked Ti-sapphire laser. *Opt. Lett.*, 16(1):42, 1991.

[38] M. T. Asaki, C. P. Huang, D. Garvey, J. Zhou, H. C. Kapteyn, and M. M. Murnane. Generation of 11-fs pulses from a self-mode-locked Ti:sapphire laser. *Opt. Lett.*, 18(12):977, 1993.

[39] W. Koechner. *Solid-State Laser Engineering.* Springer, 1996.

[40] J. I. Dadap, X. F. Hu, M. Russell, J. G. Ekerdt, J. K. Lowell, and M. C. Downer. Analysis of second-harmonic generation by unamplified, high-repetition-rate, ultrashort laser pulses at Si(001) interfaces. *IEEE J. Sel. Top. Q. Elect.*, 1(4):1145, 1995.

[41] W. Daum, H. J. Krause, U. Reichel, and H. Ibach. Identfication of strained silicon layers at Si-$SiO_2$ interfaces and clean si surfaces by nonlinear optical spectroscopy. *Phys. Rev. Lett.*, 71(8):1234, 1993.

[42] G. Erley, R. Butz, and W. Daum. Second-harmonic spectroscopy of interband excitations at the interfaces of strained Si(100)-$Si_{0.85}Ge_{0.15}$-$SiO_2$ heterostructures. *Phys. Rev. B*, 59(4):2915, 1999.

[43] G. Erley, R. Butz, and W. Daum. Erratum: Second-harmonic spectroscopy of interband excitations at the interfaces of strained Si(100)-$Si_{0.85}Ge_{0.15}$-$SiO_2$ heterostructures. *Phys. Rev. B*, 60(7):5078, 1999.

[44] J. I. Dadap, B. Doris, Q. Deng, M. C. Downer, J. K Lowell, and A. C. Diebold. Randomly oriented angstrom-scale microroughness at the Si(100)/

$SiO_2$ interface probed by optical second harmonic generation. *Appl. Phys. Lett.*, 64(16):2139, 1994.

[45] S. T. Cundiff, W. H. Knox, F. H. Baumann, K. W. Evans-Lutterodt, M. T. Tang, M. L. Green, and H. M. van Driel. $Si/SiO_2$ interface roughness: Comparison between surface second harmonic generation and x-ray scattering. *Appl. Phys. Lett.*, 70(11):1414, 1997.

[46] G. A. Reider, U. Höfer, and T. F. Heinz. Desorption kinetics of hydrogen from the Si(111)7×7 surface.

[47] P. Bratu, K. L. Kompa, and U. Höfer. Kinetics of oxygen dissociation on Si(111)7×7 investigated with optical second-harmonic generation. *Phys. Rev. B*, 49(19):14070, 1994.

[48] J. I. Dadap ad X. F. Hu, N. M. Russell, J. G. Ekerdt, M. C. Downer, and O. A. Aktsipetrov. Optical second harmonic spectroscopy of the Si(001) $E_1$ critical point resonance with variable hydrogen coverage. In *QELS '96 Summaries of Papers Presented at the Quantum Electronics and Laser Science Conference*, volume 10 of *Technical Digest Series*, page 247. Opt. Soc. America, 1996.

[49] P. S. Parkinson, D. Lim, R. Büngener, J. G. Ekerdt, and M. C. Downer. Second-harmonic spectroscopy of Ge/Si(001) and $Si_{1-x}Ge_x$(001)/Si(001). *Appl. Phys. B*, 68(3):641, 1999.

[50] D. Lim, M. C. Downer, J. G. Ekerdt, N. Arzate, B. S. Mendoza, V. I. Gavrilenko, and R. Q. Wu. Optical second harmonic spectroscopy of boron-reconstructed Si(001). *Phys. Rev. Lett.*, 84(15):3406, 2000.

[51] P. Guyot-Sionnest, P. Dumas, Y. J. Chabal, and G. S. Higashi. Lifetime of an adsorbate-substrate vibration: H on Si(111). *Phys. Rev. Lett.*, 64(18):2156, 1990.

[52] Y. J. Chabal, M. A. Hines, and D. Feijóo. Characterization of silicon surfaces and interfaces by optical vibrational spectroscopy. *J. Vac. Sci. Technol. A*, 13(3):1719, 1995.

[53] H. Ueba. Vibrational ralaxation and pump-probe spectroscopies of adsorbates on solid surfaces. *Prog. Surf. Sci.*, 55(2):115, 1997.

[54] G. Lüpke, D. J. Bottomley, and H. M. van Driel. $SiO_2$/Si interfacial structure on vicinal Si(100) studied with second-harmonic generation. *Phys. Rev. B*, 47(16):10389, 1993.

[55] G. Lüpke, D. J. Bottomley, and H. M. van Driel. Second- and third-harmonic generation from cubic centrosymmetric crystals with vicinal faces: Phenomenological theory and experiment. *J. Opt. Soc. Am. B*, 11(1):33, 1994.

[56] T. F. Heinz, M. M. T. Loy, and W. A. Thompson. Study of Si(111) surfaces by optical second-harmonic generation: Reconstruction and surface phase transformation. *Phys. Rev. Lett.*, 54(1):63, 1985.

[57] H. W. K. Tom, G. D. Aumiller, and C. H. Brito-Cruz. Time-resolved study of laser-induced disorder of Si surfaces. *Phys. Rev. Lett.*, 60(14):1438, 1988.

[58] G. Lüpke, C. Meyer, C. Ohlhoff, H. Kurz, S. Lehmann, and G. Marowsky.

Optical second-harmonic generation as a probe of electric-field-induced perturbation of centrosymmetric media. *Opt. Lett.*, 20(19):1997, 1995.

[59] J. I. Dadap ad X. F. Hu, M. ter Beek, O. A. Aktsipetrov, N. M. Russell, J. G. Ekerdt, and M. C. Downer. Applications of fs lasers to nonlinear spectroscopy and process control of Si(001) interfaces. In *Post Conference Edition. Summaries of Papers Presented at the Topical Meeting Ultrafast Phenomena*, volume 8 of *Technical Digest Series*, page 291. Opt. Soc. America, 1996.

[60] J. I. Dadap, P. T. Wilson, M. H. Anderson, M. C. Downer, and M. ter Beek. Femtosecond carrier-induced screening of dc electric- field-induced second-harmonic generation at the Si(001)-$SiO_2$ interface. *Opt. Lett.*, 22(12):901, 1997.

[61] J. G. Mihaychuk, J. Bloch, Y. Liu, and H. M. van Driel. Time-dependent second-harmonic generation from the Si-$SiO_2$ interface induced by charge transfer. *Opt. Lett.*, 20(20):2063, 1995.

[62] J. Bloch, J. G. Mihaychuk, and H. M. van Driel. Electron photoinjection from silicon to ultrthin $SiO_2$ films via ambient oxygen. *Phys. Rev. Lett.*, 77(5):920, 1996.

[63] W. Wang, G. Lüpke, M. Di Ventra, S. T. Pantelides, J. M. Gilligan, N. H. Tolk, I. C. Kizilyalli, P. K. Roy, G. Margaritondo, and G. Lucovsky. Coupled electron-hole dynamics at the Si/$SiO_2$ interface. *Phys. Rev. Lett.*, 81(19):4224, 1998.

[64] J. G. Mihaychuk, N. Shamir, and H. M. van Driel. Multiphoton photoemission and electric-field- induced optical second-harmonic generation as probes of charge transfer across the $Si/SiO_2$ interface. *Phys. Rev. B*, 59(3):2164, 1999.

[65] T. Scheidt, E. G. Rohwer, H. M. von Bergmann, and H. Stafast. Charge-carrier dynamics and trap generation in native $Si/SiO_2$ interfaces probed by optical second-harmonic generation. *Phys. Rev. B*, 69(16):165314, 2004.

[66] J. I. Dadap, Z. Xu, X. F. Hu, M. C. Downer, N. M. Russell, J. G. Ekerdt, and O. A. Aktsipetrov. Second-harmonic spectroscopy of a Si(001) surface during calibrated variations in temperature and hydrogen coverage. *Phys. Rev. B*, 56(20):13367, 1997.

[67] G. Erley and W. Daum. Silicon interband transitions observed at Si(100)-$SiO_2$ interfaces. *Phys. Rev. B*, 58(4):R1734, 1998.

[68] Y. D. Glinka, W. Wang, S. K. Singh, Z. Marka, S. N. Rashkeev, Y. Shirokaya, R. Albridge, S. T. Pantelides, N. H. Tolk, and G. Lucovsky. Characterization of charge-carrier dynamics in thin oxide layers on silicon by second harmonic generation. *Phys. Rev. B*, 65(19):193103, 2002.

[69] R. Carriles, J. Kwon, Y. Q. An, J. C. Miller, M. C. Downer, J. Price, and A. C. Diebold. Second-harmonic generation from $Si/SiO_2/Hf_{(1-x)}Si_xO_2$ structures. *submitted to Appl. Phys. Lett.*, 2005.

[70] W. L. Mochán and R. G. Barrera. Intrinsic surface-induced optical anisotropies of cubic crystals: Local-field effect. *Phys. Rev. Lett.*, 55(11):1192, 1985.

[71] W. L. Mochán and R. G. Barrera. Local-field effect on the surface conductivity of adsorbed overlayers. *Phys. Rev. Lett.*, 56(20):2221, 1986.

[72] W. L. Schaich and B. S. Mendoza. Simple model of second-harmonic generation. *Phys. Rev. B*, 45(24):14279, 1992.

[73] B. S. Mendoza and W. L. Mochán. Local-field effect in the second-harmonic-generation spectra of Si surfaces. *Phys. Rev. B*, 53(16):R10473, 1996.

[74] B. S. Mendoza and W. L. Mochán. Polarizable-bond model for second-harmonic genertion. *Phys. Rev. B*, 55(4):2489, 1997.

[75] V. I. Gavrilenko and F. Rebentrost. Nonlinear optical susceptibility of the (111) and (001) surfaces of silicon. *Appl. Phys. A*, 60(2):143, 1995.

[76] V. I. Gavrilenko and F. Rebentrost. Nonlinear optical susceptibility of the surfaces of silicon and diamond. *Surf. Sci.*, 331-333:1355, 1995.

[77] B. S. Mendoza, A. Gaggiotti, and R. Del Sole. Microscopic theory of second harmonic generation at Si(100) surfaces. *Phys. Rev. Lett.*, 81(17):3781, 1998.

[78] V. I. Gavrilenko, R. Q. Wu, M. C. Downer, J. G. Ekerdt, D. Lim, and P. Parkinson. Optical second harmonic spectra of silicon-adatom surfaces: Theory and experiment. *Thin Solid Films*, 364:1, 2000.

[79] M. C. Downer, B. S. Mendoza, and V. I. Gavrilenko. Optical second harmonic spectroscopy of semiconductor surfaces: Advances in microscopic understanding. *Surf. Interface Anal.*, 31(10):966, 2001.

[80] V. I. Gavrilenko, R. Q. Wu, M. C. Downer, J. G. Ekerdt, D. Lim, and P. Parkinson. Optical second-harmonic spectra of Si(001) with H and Ge adatoms: First-principles theory and experiment. *Phys. Rev. B*, 63(16):165325, 2001.

[81] Y. R. Shen. Optical second-harmonic generation at interfaces. *Annu. Rev. Phys. Chem.*, 40:327, 1989.

[82] Y. R. Shen. Surface properties probed by second-harmonic and sum-frequency generation. *Nature*, 337:519, 1989.

[83] Y. R. Shen. Surfaces probed by nonlinear optics. *Surf. Sci.*, 300:551, 1994.

[84] J. F. McGilp. Optical characterization of semiconductor surfaces and interfaces. *Prog. Surf. Sci.*, 49(1):1, 1995.

[85] G. Lüpke. Characterization of semiconductor interfaces by second-harmonic generation. *Surf. Sci. Rep.*, 35:75, 1999.

[86] H. W. K. Tom, T. F. Heinz, and Y. R. Shen. Second-harmonic reflection from silicon surfaces and its relation to structural symmetry. *Phys. Rev. Lett.*, 51(21):1983, 1983.

[87] O. A. Aktsipetrov, I. M. Batanova, and Y. A. Il'inskiĭ. Surface contribution to the generation of reflected second-harmonic light for centrosymmetric semiconductors. *Sov. Phys. JETP*, 64(1):167, 1986.

[88] J. I. Dadap, X. F. Hu, M. H. Anderson, M. C. Downer, J. K. Lowell, and O. A. Aktsipetrov. Optical second-harmonic electroreflectance spec-

troscopy of a Si(001) metal-oxide-semiconductor structure. *Phys. Rev. B*, 53(12):R7607, 1996.

[89] E. W. M. van der Ham, Q. H. F. Vrehen, and E. R. Eliel. Self-dispersive sum-frequency generation at interfaces. *Opt. Lett.*, 21(18):1448, 1996.

[90] P. C. Becker, H. L. Fragnito, C. H. Brito Cruz, R. L. Fork, J. E. Cunningham, J. E. Henry, and C. V. Shank. Femtosecond photon echoes from band-to-band transitions in GaAs. *Phys. Rev. Lett.*, 61(14):1647, 1988.

[91] Philip T. Wilson. *Second harmonic generation spectroscopy using broad bandwidth femtosecond pulses.* PhD thesis, The University of Texas at Austin, August 2000.

[92] R. C. Miller. Optical second harmonic generation in piezoelectric crystals. *Appl. Phys. Lett.*, 5(1):17, 1964.

[93] P. T. Wilson, Y. Jiang, R. Carriles, and M. C. Downer. Second-harmonic amplitude and phase spectroscopy by use of broad-bandwidth femtosecond pulses. *J. Opt. Soc. Am. B*, 20(12):2548, 2003.

[94] E. D. Palik. *Handbook of optical constants of solids.* Academic Press Handbook. Academic Press, 1985.

[95] U. Morgner, F. X. Kärtner, S. H. Cho, Y. Chen, H. A. Haus, J. G. Fujimoto, E. P. Ippen, V. Scheuer, G. Angelow, and T. Tschudi. Sub-two-cycle pulses from a Kerr-lens mode-locked Ti:sapphire laser. *Opt. Lett.*, 24(6):411, 1999.

[96] T. M. Fortier, D. J. Jones, and S. T. Cundiff. Phase stabilization of an octave-spanning Ti:sapphire laser. *Opt. Lett.*, 28(22):2198, 2003.

[97] H. Tanaka, G. Mizutani, and S. Ushioda. A new resonance of the surface SHG from GaAs(001) in air. *Surf. Sci.*, 402-404:533, 1998.

[98] T. A. Birks, P. J. Roberts, P. St. J. Russell, D. M. Atkin, and T. J. Shepherd. full 2-D photonic bandgaps in silica/air structures. *Elect. Lett.*, 31(22):1941, 1995.

[99] J. C. Knight, J. Broeng, T. A. Birks, and P. St. J. Russell. Photonic band gap guidance in optical fibers. *Science*, 282:1476, 1998.

[100] R. F. Cregan, B. J. Mangan, J. C. Knight, T. A. Birks, P. St. J. Russell, P. J. Roberts, and D.C. Allan. Single-mode photonic band gap guidance of light in air. *Science*, 285:1537, 1999.

[101] J. C. Knight, J. Arriaga, T. A. Birks, A. Ortigosa-Blanch, W. J. Wadsworth, and P. St. J. Russell. Anomalous dispersion in photonic crystal fiber. *IEEE Phot. Tech. Lett.*, 12(7):807, 2000.

[102] J. K. Ranka, R. S. Windeler, and A. J. Stentz. Visible continuum generation in air-silica microstructure optical fibers with anomalous dispersion at 800 nm. *Opt. Lett.*, 25(1):25, 2000.

[103] J. K. Ranka and R. S. Windeler. Nonlinear interactions in air-silica microstructure optical fibers. *Optics and Photonics News*, 11(8):20, 2000.

[104] J. C. Knight. Photonic crystal fibers. *Nature*, 424:847, 2003.

[105] T. A. Birks, W. J. Wadsworth, and P. St. J. Russell. Supercontinuum generation in taperd fibers. *Opt. Lett.*, 25(19):1415, 2000.

[106] X. Gu, L. Xu, M. Kimmel, E. Zeek, P. O'Shea, A. P. Shreenath, R. Trebino, and R. S. Windeler. Frequency-resolved optical gating and shingle-shot spectral measurements reveal fine structure in microstructure-fiber continuum. *Opt. Lett.*, 27(13):1174, 2002.

[107] J. M. Dudley, X. Gu, M. Kimmel, E. Zeek, P. O'Shea, R. Trebino, S. Coen, and R. S. Windeler. Cross-correlation frequency resolved optical gating analysis of broadband continuum generation in photonic crystal fiber: Simulations and experiments. *Opt. Express*, 10(21):1215, 2002.

[108] G. Cerullo, M. Nisoli, and S. De Silvestri. Generation of 11 fs pulses tunable across the visible by optical parametric amplification. *Appl. Phys. Lett.*, 71(25):3616, 1997.

[109] T. Wilhellm, J. Piel, and E. Riedle. Sub-20-fs pulses tunable across the visible from a blue- pumped single-pass noncollinear parametric converter. *Opt. Lett.*, 22(19):1494, 1997.

[110] H. Hwang, W. Ting, B. Maiti, D. K. Kwong, and J. Lee. Electrical characteristics of ultrathin oxynitrides gate dielectric prepared by rapid thermal oxidation of Si in $N_2O$. *Appl. Phys. Lett.*, 57(10):1010, 1990.

[111] S. V. Hattangady, H. Niimi, and G. Lucovsky. Controlled nitrogen incorporation at the gate oxide surface. *Appl. Phys. Lett.*, 66(25):3495, 1995.

[112] G. D. Wilk, R. M. Wallace, and J. M. Anthony. High-$\kappa$ gate dielectrics: Current status and materials properties considerations. *J. Appl. Phys.*, 89(10):5243, 2001.

[113] R. M. Wallace and G. Wilk. High-$\kappa$ gate dielectric materials. *MRS bulletin*, 27(3):192, 2002.

[114] P. W. Peacock and J. Robertson. Band offsets and schottky barrier heights of high dielectric constant oxides. *J. Appl. Phys.*, 92(8):4712, 2002.

[115] H. Takeuchi, D. Ha, and T. J. King. Observation of bulk $HfO_2$ defects by spectroscopic ellipsometry. *J. Vac. Sci. Technol. A*, 22(4):1337, 2004.

[116] J. Price, P. Y. Hung, T. Rhoad, B. Foran, and A. C. Diebold. Spectroscopic ellipsometry characterization of $Hf_xSi_yO_z$ films using the Cody-Lorentz parametrized model. *Appl. Phys. Lett.*, 85(10):1701, 2004.

[117] H. D. Kim, Y. Roh, Y. Lee, J. E. Lee, D. Jung, and N. E. Lee. Effects of annealing temperature on the characteristics of $HfSi_xO_y/HfO_2$ high-$\kappa$ gate oxides. *J. Vac. Sci. Technol. A*, 22(4):1347, 2004.

[118] H. Kato, T. Nango, T. Miyagawa, T. Katagiri, K. S. Seol, and Y. Ohki. Plasma-enhanced chemical vapor deposition and characterization of high-permittivity hafnium and zirconium silicate films. *J. Appl. Phys.*, 92(2):1106, 2002.

[119] S. Ramanathan, P. C. McIntyre, J. Luning, P. S. Lysaght, Y. Yang, Z. Chen, and S. Stemmer. Phase separation in hafnium silicates for alternative gate dielectrics. *J. of the Electrochem. Soc.*, 150(10):F173, 2003.

[120] H. Kim and P. C. McIntyre. Spinodal decomposition in amorphous metal-silicate thin films: Phase diagram analysis and interface effects on kinetics. *J. Appl. Phys.*, 92(9):5094, 2002.

[121] S. Stemmer, Y. Li, B. Foran, P. S. Lysaght, S. K. Streiffer, P. Fuoss, and S. Seifert. Grazing-incidence small angle x-ray scattering studies of phase separation in hafnium silicate films. *Appl. Phys. Lett.*, 83(15):3141, 2003.

[122] C. Krug and G. Lucovsky. Spectroscopic charactrization of high $\kappa$ dielectics: Applications to interface electronic structure and stability against chemical phase separation. *J. Vac. Sci. Technol. A*, 22(4):1301, 2004.

[123] S. K. Dey, A. Das, M. Tsai, D. Gu, M.Floyd, R. W. Carpenter, H. de Waard, C. Werkhoven, and S. Marcus. Relationships among equivalent oxide thickness, nanochemistry, and nanostructure in atomic layer chemical-vapor-deopisted Hf-O films on Si. *J. Appl. Phys.*, 95(9):5042, 2004.

[124] M. Copel, M. C. Reuter, and P. Jamison. Interlayer composition of $HfO_2$/ Si(001) films. *Appl. Phys. Lett.*, 85(3):458, 2004.

[125] R. Ludeke and E. Gusev. Structural and surface potential characterization of annealed $HfO_2$ and $(HfO_2)_x(SiO_2)_{1-x}$ films. *J. Appl. Phys.*, 96(4):2365, 2004.

[126] R. Ludeke, P. Lysaght, E. Cartier, E. Gusev, M. Chudzik, B. Foran, and G. Bersuker. Surface potential and morphology issues of annealed $(HfO_2)_x$ $(SiO_2)_{1-x}$ gate oxides. *J. Vac. Sci. Technol. B*, 22(4):2113, 2004.

[127] V. Fomenko, E. P. Gusev, and E. Borguet. Optical second harmonic genration studies of ultrathin high-k dielectric stacks. *J. Appl. Phys.*, 97(8):083711, 2005.

[128] K. J. Veenstra, A. V. Petukhov, A. P. de Boer, and Th. Rasing. Phase-sensitive detection technique for surface nonlinear optics. *Phys. Rev. B*, 58(24):R16020, 1998.

[129] R. Carriles, P. T. Wilson, M. C. Downer, and R. S. Windeler. Second harmonic phase spectroscopy: Frequency vs. time domain. In *OSA Trends in Optics and Photonics*, volume 73, page 449. Optical Society of America, 2002.

[130] P. T. Wilson, Y. Jiang, O. A. Aktsipetrov, E. D. Mishina, and M. C. Downer. Frequency-domain interferometric second-harmonic spectroscopy. *Opt. Lett.*, 24(7):496, 1999.

[131] K. Wu, R. Carriles, and M. C. Downer. Phase sensitive electric-field-induced second-harmonic microscopy probe of electronic materials. In *Conference on lasers and electro-optics/quantum electronics and laser science and photonic applications, systems and technologies 2004*, page CThJ3. Optical Society of America, 2004.

[132] Kui Wu. *Electric-field-induced second harmonic microscopy.* PhD thesis, The University of Texas at Austin, May 2004.

[133] D. R. Yankelevich, P. Pretre, A. Knoesen, G. Taft, M. M. Murnane, H. C. Kapteyn, and R. J. Twieg. Molecular engineering of polymer films for amplitude and phase measurements of Ti:sapphire femtosecond pulses. *Opt. Lett.*, 21(18):1487, 1996.

[134] L. Lepetit, G. Cheriaux, and M. Joffre. Linear techniques of phase measurement by femtosecond spectral interferometry for applications in spectroscopy. *J. Opt. Soc. Am. B*, 12(12):2467, 1995.

[135] M. Takeda, H. Ina, and S. Kobayashi. Fourier-transform method of fringe-pattern analysis for computer-based topography and interferometry. *J. Opt. Soc. Am.*, 72(1):156, 1982.

[136] Y. S. Lee, M. H. Anderson, and M. C. Downer. Fourth-harmonic generation at a crystalline GaAs(001) surface. *Opt. Lett.*, 22(13):973, 1997.

[137] Yun-Shik Lee. *Optical fourth harmonic generation at crystalline surfaces.* PhD thesis, The University of Texas at Austin, December 1997.

[138] C. Flueraru and P. Grover. Relative measurements of second-order susceptibility with reflective second-harmonic generation. *Appl. Opt.*, 42(33):6666, 2003.

[139] Y. Q. An and S. T. Cundiff. Bulk and surface contributions to resonant second- harmonic generation from Si(001) surfaces. *Appl. Phys. Lett.*, 81(27):5174, 2002.

[140] Y. Q. An and S. T. Cundiff. Phase inversion in rotational anisotropy of second harmonic generation at Si(001) interfaces. *Phys. Rev. B*, 67(19):193302, 2003.

[141] M. S. Yeganeh, J. Qi, A. G. Yodh, and M. C. Tamargo. Interfacial electronic trap lifetimes studied by the photomodulation of second-harmonic generation processes. *J. Opt. Soc. Am. B*, 10(11):2093, 1993.

[142] O. A. Aktsipetrov, A. A. Fedyanin, V. N. Golovkina, and T. V. Murzina. Optical second-harmonic generation induced by a dc electric field at the Si-$SiO_2$ interface. *Opt. Lett.*, 19(18):1450, 1994.

[143] O. A. Aktsipetrov, A. A. Fedyanin, J. I. Dadap, and M. C. Downer. Dc-electric-field-induced second-harmonic generation studies of surfaces and buried interfaces of column IV semiconductors. *Laser Physics*, 6(6):1142, 1996.

[144] O. A. Aktsipetrov, A.A. Fedyanin, A. V. Melnikov, E. D. Mishina, A. N. Rubtsov, M. H. Anderson, P. T. Wilson, M. ter Beek, X. F. Hu, J. I. Dadap, and M. C. Downer. dc-electric-field-induced and low-frequency electromodulation second-harmonic generation spectroscopy of Si(001)-$SiO_2$ interfaces. *Phys. Rev. B*, 60(12):8924, 1999.

[145] J. Fang and G. P. Li. Detection of gate oxide charge trapping by second-harmonic generation. *Appl. Phys. Lett.*, 75(22):3506, 1999.

[146] V. Fomenko, C. Hurth, T. Ye, and E. Borguet. Second harmonic generation investigations of charge transfer at chemically-modified semiconductor interfaces. *J. Appl. Phys.*, 91(7):4394, 2002.

[147] Y. D. Glinka, T. V. Shahbazyan, I. E. Perakis, N. H. Tolk, X. Liu, Y. Sasaki, and J. K. Furdyna. Ultrafast dynamics of interfacial electric fields in semiconductor heterostructures monitored by pump-porbe sencond- harmonic generation. *Appl. Phys. Lett.*, 81(20):3717, 2002.

[148] N. Shamir, J. G. Mihaychuk, and H. M. van Driel. Trapping and detrapping of electrons photoinjected form silicon to ultrathin $SiO_2$ overlayers. I in

vacuum and in the presence of ambient oxygen. *J. Appl. Phys.*, 88(2):896, 2000.

[149] N. Shamir and H. M. van Driel. Trapping and detrapping of electrons photoinjected form silicon to ultrathin $SiO_2$ overlayers. II in He, Ar, $H_2$, $N_2$, CO, and $N_2O$. *J. Appl. Phys.*, 88(2):909, 2000.

# Vita

Ramón Carriles Jaimes was born in Toluca, México in 1971 to Ramón Carriles Tenes and Esiolat Jaimes de Carriles. He received the Bachelor of Science degree in Physics from the Universidad Autónoma Metropolitana Iztapalapa in 1996. He started Master studies in the same university but only finished the course work because he was accepted in the PhD program of The University of Texas at Austin. He started studies in the physics program in August 1997. He is married to Estrella Sandoval de Carriles and they have a daughter, Elisa Carriles Sandoval.

Permanent address: Felipe Villanueva Sur 1212
Col. Las Haciendas
C.P. 50170 Toluca, México

This dissertation was typeset with LaTeX[†] by the author.

[†]LaTeX is a document preparation system developed by Leslie Lamport as a special version of Donald Knuth's TeX Program.